

1 High spatial resolution measurements of iron isotopes in pyrites by
2 SIMS using the new Hyperion-II Radio-Frequency Plasma source.

3
4
5 Marie-Noëlle Decraene^{1,2*}, Johanna Marin-Carbonne¹, Anne-Sophie Bouvier¹, Johan
6 Villeneuve², Nordine Bouden², Béatrice Luais² and Etienne Deloule².

7
8
9 ¹Institut des Sciences de la Terre, Université de Lausanne, Lausanne, Suisse.

10 ² Université de Lorraine, CNRS, CRPG, F-54000 Nancy, France.

11 *Corresponding author contact: marie-noelle.decraene@unil.ch

12
13
14
15
16
17
18
19
20
21
22
23
24
25
26
27 **Key words:** Iron isotopes; Ion microprobe; Pyrites.

28 **Abbreviations:** SIMS: Secondary Ions Mass Spectrometry; MC-ICP-MS: Multi-collector
29 inductively coupled plasma mass spectrometry; IMF: Instrumental Mass Fractionation; SD:
30 Standard Deviation; SE: Standard Error.

31

32 **Abstract**

33 **Rationale:** Iron isotopic signatures in pyrites are considered as a good proxy to reconstruct
34 paleoenvironmental and local redox conditions. However, the investigation of micro-pyrites
35 less than 20 μ m size has been limited so far by analytical techniques. The development of the
36 new brighter radio-frequency plasma ion source (Hyperion-II source) enhances the spatial
37 resolution by increasing the beam density 10 times compared to the Duoplasmatron source.

38 **Methods:** Here we present high spatial resolution measurements of iron isotopes in pyrites
39 using a 3nA-3 μ m primary $^{16}\text{O}^-$ beam on two ion microprobes Cameca IMS 1280-HR2 at
40 CRPG-IPNT (France) and at SwissSIMS (Switzerland) equipped with Hyperion sources. We
41 tested analytical effects, such as topography and crystal orientation that could induce
42 analytical biases perceptible through variations of the Instrumental Mass Fractionation (IMF).

43 **Results:** The $\delta^{56}\text{Fe}$ reproducibility for the Balmat pyrite standard is $\pm 0.25\%$ (2SD, standard
44 deviation) and the typical individual internal error is $\pm 0.10\%$ (2SE, standard error). The
45 sensitivity on $^{56}\text{Fe}^+$ was 1.2×10^7 cps/nA/ppm or better. Tests on Balmat pyrites revealed that
46 neither the crystal orientation nor channeling effects seem to significantly influence the IMF.
47 Different pyrite standards (Balmat and SpainCR) were used to test the accuracy of the
48 measurements. Indium mounts must be carefully prepared with sample topography $< 2\mu\text{m}$,
49 which was checked using an interferometric microscope. Such a topography is negligible for
50 introducing change in the IMF. This new source increases the spatial resolution while
51 maintaining the high precision of analyses and the overall stability of the measurements
52 compared to the Duoplasmatron source.

53 **Conclusions:** We developed a reliable method to perform accurate and high-resolution
54 measurements of micrometric pyrites. The investigation of sedimentary micro-pyrites will
55 improve our understanding of the processes and environmental conditions during pyrite
56 precipitation, including contribution of primary (microbial activities or abiotic reactions) and
57 secondary (diagenesis and/or hydrothermal fluid circulation) signatures.

58

59 1. Introduction

60 Iron stable isotope geochemistry has been developed rapidly over the last 15 years,
61 particularly because iron is a ubiquitous element that occurs in three oxidation states: Fe⁰,
62 Fe²⁺ and Fe³⁺. The redox state affects iron isotope fractionation of the four stable isotopes,
63 ⁵⁴Fe (5.80%), ⁵⁶Fe (91.72%), ⁵⁷Fe (2.20%) and ⁵⁸Fe (0.28%), following the mass- and
64 temperature-dependent fractionation laws¹⁻⁴. The iron isotopic composition is reported using
65 the delta (δ) notation (in ‰) defined as deviations of the measured ⁵⁶Fe/⁵⁴Fe or ⁵⁷Fe/⁵⁴Fe
66 ratios of the sample relative to the international standard IRMM-014 (⁵⁶Fe/⁵⁴Fe value of
67 15.6986 and ⁵⁷Fe/⁵⁴Fe=0.3626)^{5,6} :

68

$$69 \quad \delta^{5x}Fe = \left[\frac{\left(\frac{{}^{5x}Fe}{{}^{54}Fe}_{sample} \right)}{\left(\frac{{}^{5x}Fe}{{}^{54}Fe}_{IRMM014} \right)} - 1 \right]$$

70 where x is either 6 or 7. Accuracy and precision were determined by the analysis of in-house
71 pyrite standards, Balmat and SpainCR (detailed in section 2.1).

72 The difference of Fe isotopic compositions between 2 species defines the isotopic
73 fractionation. Iron isotope systematics is used in numerous fundamental fields, such as in
74 cosmochemistry and igneous petrology that focus on the accretion of planetary bodies,
75 magmatic differentiation, and diffusion during crystal growth^{5,7-11}, as well as in
76 environmental geochemistry for understanding the past and modern redox marine cycle^{5,12-17}.
77 Iron is also a major element in numerous biological reactions leading to diagnostic isotopic
78 fractionations and thus, can be a good proxy for biosignature recognition. The microbial iron
79 cycle is controlled by Dissimilatory Iron Reduction (DIR) and bacterial iron oxidation
80 leading to precipitation of diverse Fe(II)-bearing biominerals, including iron sulfides^{18,19}.
81 However, pyrites can also be formed through abiotic reactions. Both biological and abiotic
82 pathways are associated with large mass-dependent Fe isotopic fractionations²⁰⁻³³.
83 Consequently, biologically-precipitated pyrites record δ⁵⁶Fe variations up to 6‰^{20,22-24},
84 encompassing the entire range of terrestrial Fe isotopic fractionation (see e.g., Johnson et al,¹³
85 and Beard and Johnson,³⁴ for reviews). The formation of sedimentary pyrites is a complex,
86 multi-stage process that includes dissolution of FeS_m precursors such as mackinawite (FeS)
87 or greigite (Fe₂S₃) e.g. ^{35,36}. Importantly, biologically-mediated sulfides are typically very
88 small, <1µm in size, as illustrated by FeS precipitates in microbial sulfate reducing bacteria
89 cultures (reviewed in Rickard³⁷). The dissolution of those FeS precursors leads to the

90 precipitation of pyrites ranging from <1 to tens of micrometers in size (especially for
91 sedimentary pyrite framboids)³⁸, which induce analytical challenges for isotopic
92 measurements in a single pyrite grain.

93 Investigation of iron isotope variability started with application of Thermal Ionization
94 Mass Spectrometry (TIMS) and was subsequently followed by Multi Collection Inductively
95 Coupled Plasma Mass Spectrometry (MC-ICPMS) yielding higher sensitivity and higher
96 precision measurements. As a result, the application of MC-ICPMS method on igneous rocks
97 allowed the recognition of small iron isotope variations associated with high temperature
98 fractionation processes^{8,32,33}. However, only few studies focused on microscale isotope
99 variations in biogeochemistry. For instance, depending of the technique, strong contrasts in
100 Fe isotope compositions have been documented in pyrites from the 2.7 Ga Tumbiana
101 Formation (Pilbara craton, Western Australia). Bulk rock analyses produced a narrow range
102 of $\delta^{56}\text{Fe}$ values of $-0.02 \pm 0.26\text{‰}$ (2SD, standard deviation)¹⁵, while *in situ* analyses by LA-
103 MC-ICPMS (Laser Ablation Multi Collector Inductively Coupled Plasma Mass
104 Spectrometry) yielded a large range of $\delta^{56}\text{Fe}$ values, from -2.9‰ to $+1.5\text{‰}$ ^{39,40}. Similarly, in
105 Archean pyrite nodules (2.7 Ga shale from Bubi Greenstone Belt, Zimbabwe), bulk $\delta^{56}\text{Fe}$
106 values were around -1.4‰ whereas *in situ* measurements by Secondary Ion Mass
107 Spectrometry (SIMS) described rim to core profiles from $+0.5\text{‰}$ to -2‰ ¹⁶. These two
108 examples strongly support the importance of combining whole rocks and micrometer scale *in*
109 *situ* analysis to constrain primary and/or secondary signals recorded in a pyrite.

110 Available on the market since 2015, the new radio-frequency oxygen ion source on
111 SIMS instruments, the Hyperion-II, has the primary beam current density improved 10 times
112 compared to the usual Duoplasmatron oxygen source⁴¹. Characteristics of the primary beam
113 and secondary transmission are documented in Liu et al.⁴¹. For a given primary beam
114 intensity, the improvement of current density increases spatial resolution while maintaining
115 analytical precision compared to the previous $^{16}\text{O}^-$ source performance. The improvement of
116 the secondary ion transmission, higher precision and reproducibility measurements have been
117 reported for $\text{Mg}^{41,42}$ and Si^{43} isotope systems. For example, an external reproducibility of
118 $\pm 0.2\text{‰}$ (2SD) on $\Delta^{26}\text{Mg}^*$ (independent mass fractionation) is achieved with a primary beam
119 size of $3\text{-}4\mu\text{m}^{41}$, much smaller compared to $15\mu\text{m}$ with the Duoplasmatron source⁴⁴. The new
120 source has also higher sensitivity per unit area for Pb isotopes with a 10nA primary beam,
121 allowing the precision of U-Pb dating measurements of zircons to be enhanced⁴¹. Therefore,
122 one of the main advantages of the Hyperion source is the improved spatial resolution
123 achieved without a loss in precision required for resolving biogeochemical processes.

124 Previously, the expected precision of $\pm 0.2\%$ (2SD) for iron isotope analysis was obtained
125 with a 10nA primary intensity delivered by the Duoplasmatron, focused into a $\sim 15\mu\text{m}$ spot to
126 generate enough secondary ion intensity to be collected by Multi Collection Faraday Cups
127 (MCFC). However, such spot sizes limited the investigation of Fe isotopes in micrometric
128 grains, whereas the Hyperion source opens new possibilities for the studies of biochemical
129 processes.

130 In order to explore micrometric scale variations of iron isotope in pyrites, we have
131 adapted a previously described analytical procedure by using the Hyperion source, combining
132 the reduction of the spot size for a given intensity, and maintaining a precision of 0.2%
133 (2SD). This protocol has been tested on two different SIMS instruments and will open a new
134 analytical field to study iron isotope microscale variabilities in sedimentary pyrites.

135

136 2. Experimental

137 SIMS measurements were carried out using the Cameca[®] IMS 1280-HR2 ion probes
138 at CRPG-IPNT (Nancy, France) and SwissSIMS (University of Lausanne, Switzerland), both
139 equipped with the new Hyperion-II Radio frequency source. We performed four Fe isotope
140 sessions at CRPG-IPNT (February 2018, April 2018, July 2018 and September 2020) and
141 four sessions at SwissSIMS (July 2019, January 2020, March 2020 and June 2020).

142

143 2.1. Standards

144 The stability of both instruments was monitored by running multiple measurements of
145 in-house pyrite standards, either Balmat or SpainCr pyrites, that were also used to correct a
146 possible instrumental drift. The major element composition of Balmat pyrite is described in
147 Marin-Carbonne et al.⁴⁵ and it contains 46.5wt.% of iron and 53.6wt.% of S. This pyrite
148 standard is extensively used for SIMS Fe and S isotopes analyses^{16,45-47}. The major and trace
149 element compositions of SpainCR pyrite was determined using a JEOL JXA-8530F electron
150 microprobe at the University of Lausanne and data are available in **supporting information**
151 **A**. The analytical parameters are described in **supporting information B**. SpainCR pyrite
152 grains contain 46.6wt.% of Fe and 53.1wt.% of S. Co, Mn, Cr, Zn and Cu contents are below
153 the detection limit. Pb, Ti and Ni contents are 1112ppm, 1003ppm and 354ppm, respectively.
154 The SpainCR standard was previously used for SIMS S isotope analysis^{47,48}. The Fe isotopic
155 composition of SpainCR pyrite was determined at CRPG. Chemistry for Fe purification, and
156 Fe isotopic analysis using the NeptunePlus MC-ICP-MS are detailed elsewhere^{45,49,50}. In
157 order to evaluate the homogeneity of Fe isotopic composition of SpainCR pyrite standard,

158 core and rim separates have been chemically processed and analyzed. The bulk Fe isotope
159 measurement sequence follows the sample/standard bracketing method, with IRMM-014 Fe
160 as the normalizing standard. We obtained similar $\delta^{56}\text{Fe}$ (and $\delta^{57}\text{Fe}$) values of $+0.516 \pm 0.05\text{‰}$
161 ($+0.804 \pm 0.03\text{‰}$) (2SD) and $+0.521 \pm 0.02\text{‰}$ ($+0.795 \pm 0.01\text{‰}$) (2SD) for core and rim,
162 respectively, for $n=3$ replicates of each. This gives a $\delta^{56}\text{Fe}_{\text{mean}}$ reference value of 0.52
163 $\pm 0.03\text{‰}$ for this highly homogeneous SpainCR pyrite standard. Data accuracy and 2SD
164 reproducibility are evaluated by replicate analyses of geostandards, with values of $\delta^{56}\text{Fe} =$
165 $+0.648 \pm 0.129 \text{‰}$ and $\delta^{57}\text{Fe} = +0.960 \pm 0.163\text{‰}$ ($n=3$) for IF-G (BIF Greenland), and $\delta^{56}\text{Fe} =$
166 $+0.098 \pm 0.033\text{‰}$ and $\delta^{57}\text{Fe} = +0.143 \pm 0.057\text{‰}$ ($n=15$) for BIR-1 (USGS Iceland basalt)
167 during the course of this study. These values are within the range of the reported reference
168 values⁵. The homogeneity of SpainCR standard was tested by SIMS by measuring three
169 different grains prepared in the same mount (July 2018 session at CRPG-IPNT). Based on 68
170 measurements, the external reproducibility was $\pm 0.28\text{‰}$ (2SD) (**Figure S1, supporting**
171 **information B**).

172 As no chromium was detected in the pyrite reference materials, Russie magnetite
173 standard was used to evaluate the degree of ^{54}Cr interference on ^{54}Fe , which was necessary
174 for the natural samples due to the presence of Cr. Details are given in section 2.5.

175

176 *2.2. Sample preparation*

177 Standard grains were embedded in epoxy and polished with $0.5\mu\text{m}$ diamond paste.
178 Those grains were carefully removed from epoxy and pressed into 1-inch indium mount.
179 White light interferometric microscope (Bruker Contour GTK at University of Lausanne) was
180 used to measure the sample topography. The relief across the analyzed surface was below
181 $5\mu\text{m}^{51}$. Samples were coated with a 35nm thick gold film to ensure the conductivity between
182 the sample surface and the SIMS holder.

183

184 *2.3. Electron backscatter diffraction (EBSD):*

185 In order to check for the influence of crystallographic orientations on SIMS
186 measurements, three Balmat pyrite grains were removed from the Indium mount, embedded
187 in epoxy resin with the analyzed mineral surfaces facing upwards. To eliminate any residual
188 surface damage, the mount was further polished for 40 min using the combined chemical and
189 mechanical effect of an alkaline ($\text{pH}=9.8$) suspension of colloidal silica ($0.05 \mu\text{m}$). The
190 sample was not carbon-coated before electron backscatter diffraction (EBSD) analysis in

191 order to maximize the detected signal. The crystallographic orientation patterns were
192 acquired at the University of Lausanne, Switzerland, using a Tescan Mira II LMU field
193 emission-scanning electron microscope (FE-SEM) equipped with the Symmetry detector and
194 the Aztec 4.2 software package, both released by Oxford Instruments®. Acquisition
195 parameters included an acceleration voltage of 20 kV, a probe current of 1.1 nA, a working
196 distance of 23 mm, and a 70° tilt of the sample surface with respect to the horizontal. As
197 pyrite has a cubic crystal structure, [100], [010], and [001] axes are equivalent and
198 orthogonal, and the maximum misorientation imposed by symmetry is 62.8°. The pyrite
199 (m3)⁵³ match unit (a = 5.4166Å) was used as a reference file for the indexing of the EBSD
200 patterns, the high quality of which was attested by a mean angular deviation (MAD) value
201 ranging between 0.2 and 0.6. Six to ten EBSD patterns per grain were collected and the
202 average crystallographic orientations represented in an upper hemisphere equal area pole
203 figure of Euler angle triplets (ϕ_1, Φ, ϕ_2). For more information on the basics of the EBSD
204 technique, the reader is referred to Prior et al.⁵³.

205

206 2.4. SIMS settings:

207 The samples were stored in the vacuum chamber at 2.5×10^{-8} mbar to 2×10^{-9} mbar.
208 Samples were sputtered with a 3nA $^{16}\text{O}^-$ primary beam accelerated by a 13kV high voltage.
209 The corresponding spot size was 2.5µm to 3µm (**Figure 2**). The primary beam was mainly
210 focused through L3 and L4 lenses of the primary column in Gaussian mode and the
211 aberration was reduced by using a PBMF aperture of 200µm. The L4 aperture was
212 maintained open at 750µm. These settings of primary beam apertures were the same for both
213 instruments and the main SIMS settings are summarized in **Table 1**. The entrance slit was set
214 to 61µm at SwissSIMS and 85µm at CRPG-IPNT, corresponding to a mass resolving power
215 (MRP) of $M/\Delta M \sim 6700-7000$ (slit 3) at SwissSIMS and $M/\Delta M \sim 6100$ (slit 3) at CRPG-IPNT
216 resolving the interference of $^{53}\text{CrH}^+$ on $^{54}\text{Fe}^+$ ($M/\Delta M = 6088$). The interference of $^{54}\text{Cr}^+$ on
217 $^{54}\text{Fe}^+$ (MRP~74,000) was monitored by analyzing $^{52}\text{Cr}^+$ as described elsewhere⁴⁵. Although
218 pyrite standards have no detectable Cr, hundreds to a thousand of counts of ^{52}Cr are measured
219 in natural pyrites, calling for a need to estimate the $^{54}\text{Cr}^+$ contribution at mass 54 and then
220 correct for it. The correction scheme for Cr was established using a magnetite standard,
221 which has a detectable amount of Cr, resulting in a final correction of ~0.15‰ on $\delta^{56}\text{Fe}$ per
222 1×10^4 counts per second (cps) of $^{52}\text{Cr}^+$. The interference of $^{56}\text{FeH}^+$ on $^{57}\text{Fe}^+$, which requires a
223 MRP of 7700 could not be clearly resolved with the chosen slit settings. However, this high
224 spatial resolution method is developed in order to analyze $\delta^{56}\text{Fe}$ values in micrometric

225 pyrites. To obtain a maximum internal error of 0.3‰ (2SE standard error) on $\delta^{56}\text{Fe}$, the
226 minimum $^{56}\text{Fe}^+$ intensity on the pyrite standard should be 4×10^7 cps, which cannot be attained
227 under $\text{MRP} > 7000$. Pyrite being nominally anhydrous mineral held under the chamber
228 vacuum of $\sim 2 \times 10^{-9}$ mbar yields low interferences of $^{56}\text{FeH}^+$ with the $^{57}\text{Fe}^+$. When pyrites are
229 prepared in an indium mount, the iron hydride was not detected on the faraday cup (FC)
230 measurements (see section 2.5). The secondary ion beam was filtered by an energy slit of 50
231 eV. A $2000 \mu\text{m}$ square field aperture was used to clip $\sim 10\%$ of the signal and to remove off-
232 axis aberrations of the secondary ion beam. We used a transmission setting (Maximum Area
233 (MA) 80) leading to a field of view of the sample of $20 \times 20 \mu\text{m}$ in the field aperture. The
234 secondary $^{54}\text{Fe}^+$, $^{56}\text{Fe}^+$, $^{57}\text{Fe}^+$ and $^{52}\text{Cr}^+$ ions were accelerated at 10kV and analyzed on three
235 off-axis FCs and one electron multiplier (EM) (detectors C, H1, H'2 and L2 respectively).
236 The C and H1 FCs were equipped with $10^{11} \Omega$ resistors. The H'2 FC was equipped with a
237 $10^{12} \Omega$ resistor at CRPG-IPNT and a $10^{11} \Omega$ resistor at SwissSIMS. The relative yields of the
238 amplifiers of the FCs were calibrated before each session on both ion microprobes and the
239 background noises of the FCs were measured for each analysis. The high voltage of the EM
240 (EM HV) was adjusted before each session. No aging effect of the EM was observed during
241 the session. Presputtering time is necessary to remove the 35nm of gold and potential surface
242 contamination, to implant primary ions in the sample surface and to get a stable secondary
243 signal. The intensity of $^{56}\text{Fe}^+$ increased until it became stable after 90s (**Figure S2,**
244 **supporting information B**). The intensity of the signal is then stable with a typical count
245 rate between 4×10^7 and 5×10^7 cps when using a 3nA primary beam intensity.

246 The analytical routine then consisted of 90s of presputtering followed by 60 cycles (5s
247 each) of collection separated by 0.08s waiting time, for a total of 7 min per analysis. After
248 presputtering, automatic beam centering in the field and contrast apertures, the energy slit and
249 transfer deflectors were performed routinely. The typical count rate of $^{54}\text{Fe}^+$, $^{56}\text{Fe}^+$ and $^{57}\text{Fe}^+$
250 are 3.2×10^6 , 4.8×10^7 and 1.1×10^6 cps respectively for Balmat reference material measured at
251 the SwissSIMS instrument tuned with a primary beam intensity of 3.05nA and 4.3×10^6 ,
252 6.4×10^7 and 1.4×10^6 cps, respectively, at the CRPG-IPNT instrument tuned with a primary
253 beam intensity ranging from 3.2 to 3.5nA (**Table 1**). The difference in ion counting
254 intensities between the two instruments is due to the higher primary current set at CRPG-
255 IPNT and also reflects a differential transmission due to the use of a larger entrance slit at
256 CRPG-IPNT. The internal precision on $\delta^{56}\text{Fe}$ of Balmat standard was $\pm 0.10\%$ (2SE). The
257 reproducibility is reported in terms of 2SD, standard deviation. The external reproducibility

258 ranges between $\pm 0.24\%$ (n=33) to $\pm 0.30\%$ (n=17, 2SD) at CRPG-IPNT and from
259 $\pm 0.15\%$ (n=10) to $\pm 0.28\%$ (n=39, 2SD) at SwissSIMS (**Table 2**).

260

261 *2.5. Mass Interferences ($^{53}\text{CrH}^+$ and $^{56}\text{FeH}^+$):*

262 The required MRP to resolve the isobaric interference of $^{54}\text{Cr}^+$ on $^{54}\text{Fe}^+$ is out of the
263 ion microprobe capabilities (MRP \sim 74,000), thus, the interference was indirectly quantified
264 by measuring $^{52}\text{Cr}^+$. The detailed procedure for Cr correction⁴⁵ shows that the $^{53}\text{Cr}/^{52}\text{Cr}$ ratio
265 measured by SIMS is similar to that determined from Cr isotopes natural abundances
266 ($^{52}\text{Cr}=83.8\%$, $^{53}\text{Cr}=9.5\%$ and $^{54}\text{Cr}=2.4\%$). We thus used the natural abundances of Cr
267 isotopes combined with the measured $^{52}\text{Cr}^+$ intensity to calculate the $^{54}\text{Cr}^+$ intensity in
268 standards and samples and then corrected the ^{54}Cr contribution from the measured ^{54}Fe
269 signal. The $^{53}\text{CrH}^+$ peak height was measured in Russie magnetite standard, on the axial EM
270 (monocollection mode), using a 800pA primary beam intensity to obtain $\sim 2 \times 10^5$ cps on $^{54}\text{Fe}^+$
271 and to not saturate the detector. Under a vacuum of 3.4×10^{-9} mbar, $^{53}\text{CrH}^+$ peak represents less
272 than 0.05% of the $^{54}\text{Fe}^+$ peak (**Figure 1A**). Tens of counts are detected for $^{52}\text{Cr}^+$ in pyrite
273 standards using a 3nA primary beam, meaning that this hydride contribution can be ignored.

274 Accuracy of analysis can also be impacted by the interference of $^{56}\text{FeH}^+$ on $^{57}\text{Fe}^+$. In
275 this study, the MRP was set lower (~ 6800) than that required to separate these two species.
276 Getting a higher MRP to have accurate $\delta^{57}\text{Fe}$ data would decrease the precision of $^{56}\text{Fe}/^{54}\text{Fe}$
277 ratios. However, the contribution from $^{56}\text{FeH}^+$ hydride has been measured to evaluate the
278 reliability of $^{57}\text{Fe}/^{54}\text{Fe}$ ratios. High resolution scan (MRP 7800) of the mass ^{57}Fe was carried
279 out on the axial EM using a 1nA primary beam intensity (**Figure 1C**). The magnitude of
280 $^{56}\text{FeH}^+$ peak is 0.05% of the $^{57}\text{Fe}^+$ peak height due to good vacuum conditions in the analysis
281 chamber ($\sim 3.4 \times 10^{-9}$ mbar) but can be up to 0.2% of the $^{57}\text{Fe}^+$ peak height when vacuum
282 conditions deteriorate to 2×10^{-8} mbar. The level of $^{56}\text{FeH}^+$ formation is thus estimated to
283 0.01%-0.04%. At MRP 6800, the mass scan shows that ^{57}Fe flat top is affected by the tail of
284 the hydride peak (**Figure 1B**). The hydride contribution on ^{57}Fe signal is thus insignificant
285 for measurements done in indium mounts. The contribution of hydrides to the Fe isotopic
286 signal, in particular the interference of $^{56}\text{FeH}^+$ with $^{57}\text{Fe}^+$, can also be evaluated by the
287 relationship between the $^{56}\text{Fe}/^{54}\text{Fe}$ and $^{57}\text{Fe}/^{54}\text{Fe}$ ratios. Pyrites from sedimentary rocks
288 (Sonoma basin, USA) and standards (Balmat pyrite) measured during the July 2020 session
289 are plotted in a three-isotopes diagram using the natural logarithm of the measured $^{56}\text{Fe}/^{54}\text{Fe}$
290 and $^{57}\text{Fe}/^{54}\text{Fe}$ ratios (**Figure 1D**, data available in **Table S1**, **supporting information B**). All
291 the data define a slope of 0.679 (± 0.007) with a correlation coefficient r^2 of 0.987, which is

292 consistent with the expected mass-dependent fractionation slope of 0.678. Since the measured
293 slope is consistent with the terrestrial mass fractionation slope, the contribution of $^{56}\text{FeH}^+$ to
294 the $^{57}\text{Fe}/^{54}\text{Fe}$ ratio is assumed negligible. Sample mounting using indium rather than epoxy
295 together with vacuum conditions below 5×10^{-9} mbar are crucial for maintaining small hydride
296 contributions and to produce reliable $\delta^{57}\text{Fe}$ data and high precision $\delta^{56}\text{Fe}$ values.

297

298 *2.6. IMF correction:*

299 The effect of a mass dependent fractionation due to the instrument, or instrumental
300 mass fractionation (IMF), is defined as:

301
$$\alpha_{inst} = \frac{\left(\frac{^{56}\text{Fe}}{^{54}\text{Fe}}\right)_{measured}}{\left(\frac{^{56}\text{Fe}}{^{54}\text{Fe}}\right)_{true}} \text{ or } \Delta^{56}\text{Fe } inst (\text{‰}) = \delta^{56}\text{Fe } measured - \delta^{56}\text{Fe } true \text{ by using the}$$

302 approximation $\Delta^{56}\text{Fe}_{inst} \approx \ln(\alpha_{inst})$.

303 The “measured” and “true” $\delta^{56}\text{Fe}$ values are iron isotopic composition measured in the
304 same reference material by SIMS and MC-ICP-MS. The typical IMF on pyrite is $\sim -30 \pm 5\%$,
305 measured by both Hyperion-II and Duoplasmatron sources but the exact value depends on the
306 instrument tuning. For example, a 4‰ shift in the IMF for Balmat pyrite was measured after
307 retuning of the primary beam. Slight modifications of the primary beam (i.e. different high
308 voltages on the primary lenses resulting in similar primary intensity but different beam
309 densities) and entrance slit settings lead to the variation of the IMF on Balmat pyrite between
310 -31.20 and -33.10% at CRPG-IPNT and highly variable, from -27.23 to -35.16% at
311 SwissSIMS (**Table 2**). We measured the IMF using Balmat pyrite standard to monitor the
312 stability of the ion probe during each session.

313

314 **3. Results and discussion**

315

316 *3.1. Spot size:*

317 The resolution of ion images of a silicon grid on an electron multiplier is used to
318 estimate the $^{16}\text{O}^-$ primary beam size. To find the best possible resolution of the image, (i.e.,
319 getting the smallest beam) we tested different combinations of primary lenses, and the best
320 result was obtained by setting the voltage on L1 and L2 to 9800V and 9900V, respectively,
321 and keeping the L3 close to 8500V. The results of the $^{30}\text{Si}^+$ ion images are reported in **Figure**
322 **2A**. Using a 3nA $^{16}\text{O}^-$ beam, the ability to differentiate two silicon bars on the $3\mu\text{m}$ grid
323 indicates a spot comparable to $3\mu\text{m}$ size. The $2\mu\text{m}$ gap between the two horizontal Si bars is

324 not completely resolved whereas the vertical bars are clearly visible, meaning the spot size is
325 between 2.5 and 3 μ m. The spot size was verified with a scanning electron microscope (SEM)
326 (**Figure 2B**) and an interferometric microscope (**Figure 2C**) after the SIMS measurements of
327 a sedimentary micro-pyrite and the pyrite standard (Balmat). White light interferometric
328 microscopy allows for the precise quantification of the beam size, by imaging the relief of the
329 beam crater in both X and Y directions (**Figures 2C and 2D**). The primary beam size is
330 measured at the bottom of the pit and corresponds to a \sim 3 μ m diameter spot. This quantitative
331 analysis is consistent with the beam size estimated through ion imaging of the Si grid. The
332 sputtered area is extended over a diameter of 6 x 7-9 μ m depending on the session and the pit
333 is \sim 3 μ m deep (**Figure 2D**). The asymmetric shape of the crater and the larger sputtered area
334 compared to the real primary beam size are due to the incidence angle of the beam with the
335 sample surface, which is characteristic of the Cameca[®] ion probes (except NanoSIMS)
336 (**Figure 2B**).

337

338 *3.2. Crystal orientation and topography effects on instrumental mass fractionation* 339 *(IMF):*

340 The IMF is the main limitation in the accuracy of SIMS analysis^{54,55}. It results from
341 various processes occurring during secondary atom ionization, extraction, secondary ion
342 transmission and detection⁵⁵. The IMF is known to be greatly dependent on the sample
343 characteristic (mineralogy, chemical composition and crystallographic orientation⁵⁵⁻⁵⁷). This
344 effect is corrected by measuring reference material (same mineral, crystallography and major
345 element chemical compositions) and samples in the same analytical conditions. The IMF
346 variations occur in various isotopic systems, for example, the $\delta^{18}\text{O}$ measurements of garnets
347 are strongly affected by their Ca-Fe-Mg content^{58,59}, as well as $\delta^{34}\text{S}$ in Fe-Ni sulfides^{56,60,61},
348 and Mg and Si isotopes in silicates (e.g. olivine, glass, pyroxene) with an IMF depending on
349 their Mg content^{43,62}. Crystal orientation may also have in some cases a strong influence on
350 the IMF, as demonstrated for example on Fe isotopic compositions in magnetite⁵⁷, on S
351 isotope compositions in sphalerite and galena⁶³ and on U-Pb dating in baddeleyite⁴.

352 As pyrites are not affected by major element substitution, *i.e.* no solid solution or
353 chemical variability, the potential variations of the IMF can only be the result of the crystal
354 orientation and/or the topography. The EBSD pole figure shown in **Figure 3B** displays the
355 crystallographic orientations of the three different grains of Balmat standard projected on a
356 plane (XY) parallel to the surfaces analyzed by SIMS (and EBSD). With misorientation
357 angles between [100] axes in Grain 1, 2, and 3 (G1-G3) and the reference direction Z (*i.e.* the

358 normal to the page pointing towards the reader) of 14°, 6°, and 1°, respectively, the analyzed
359 surfaces can be considered nearly parallel to the face of the pyrite unit cell (i.e. normal to the
360 [100] axis). The misorientation angle between the [100] axes located in the middle of the pole
361 figure is 18° between G1 and G2, and 15° between G1 and G3. Fe isotopic measurements
362 show respective mean $\delta^{56}\text{Fe}$ values and external reproducibility of $-0.29 \pm 0.30\text{‰}$ (2SD) /
363 $\pm 0.13\text{‰}$ (2SE, n=5), $-0.59 \pm 0.42\text{‰}$ (2SD) / $\pm 0.19\text{‰}$ (2SE, n=5) and $-0.32 \pm 0.44\text{‰}$ (2SD) /
364 $\pm 0.20\text{‰}$ (2SE, n=5), for G1, G2, and G3 (**Figure 3A**). Those $\delta^{56}\text{Fe}$ values suggest that the
365 inter-grain variability is lower than the reproducibility (2SD) and the uncertainty on the
366 averages (2SE). Even though the EBSD measurements on a sample set of only three grains
367 have no statistical significance, it can be said at this stage that no obvious relationship
368 between the crystallographic orientation of pyrite and SIMS $\delta^{56}\text{Fe}$ measurements has been
369 observed. A thorough review (beyond the scope of this study) based on a wide range of
370 crystallographic orientations is needed to confirm this initial statement. Our results are also
371 consistent with the absence of crystal orientation effects on S isotopes^{57,65}.

372 The channeling effect of the primary ion beam as a function of atomic planes
373 orientation has been shown to influence the secondary ion yields and thus the instrumental
374 mass fractionation^{66,67}. Similarly to magnetite that exhibits channeling effects and plane-
375 specific IMF for Fe and O isotopes⁵⁷, pyrites are cubic minerals that could experience similar
376 effects. This effect was evaluated by rotating the mount in the sample holder by 90°, 180°
377 and 270°. We ran 3 to 6 analyses per rotation (**Table S2, supporting information B**). The
378 mean IMF-corrected $\delta^{56}\text{Fe}_{\text{IRMM014}}$ values for P0, P1, P2 and P3 are $-0.38 \pm 0.31\text{‰}$ (2SD) /
379 $\pm 0.13\text{‰}$ (2SE, n=6) for P0, $-0.49 \pm 0.37\text{‰}$ (2SD) / $\pm 0.21\text{‰}$ (2SE, n=3) for P1, $-0.38 \pm 0.12\text{‰}$
380 (2SD) / $\pm 0.07\text{‰}$ (2SE, n=3) for P2 and $-0.39 \pm 0.36\text{‰}$ (2SD) / $\pm 0.16\text{‰}$ (2SE, n=5) (**Figure**
381 **4**). Considering the external reproducibility (2SD) and the internal error (2SE) together, those
382 data show a similar mean $\delta^{56}\text{Fe}$ values across the four positions in the holder.

383 Surface topography could also induce artificial iron isotopic variations, especially
384 when pyrite grains are just slightly bigger than the primary spot size. Here, a core to rim
385 profile on Balmat pyrites was performed in order to examine the edge effect on the reliability
386 of $\delta^{56}\text{Fe}$ analyses. Fe isotope analyses show similar $\delta^{56}\text{Fe}$ values between the core and the rim
387 of $\delta^{56}\text{Fe}_{\text{BalmatPf1@01}} = -0.27 \pm 0.11\text{‰}$ (2SE, n=1, core) and $\delta^{56}\text{Fe}_{\text{BalmatPf1@8}} = -0.28 \pm 0.12\text{‰}$ (2SE,
388 n=1, rim) and an external reproducibility of $\pm 0.18\text{‰}$ (2SD) (**Figure 5D**, data available in
389 **Table S2 supporting information B**). This profile (Pf1) is characterized by a topographic
390 difference of 1.7 μm (**Figure 5C**), which is not significant to introduce a bias. However, the
391 last analysis is located at $\sim 20\mu\text{m}$ from the grain edge that is $\sim 7\mu\text{m}$ above the enclosing

392 indium. Thus, this value was measured in the slightly tilted shade zone on the edge of the
393 pyrite (**Figure 5A and Figure 5B**), demonstrating the reliability of $\delta^{56}\text{Fe}$ values.

394

395 3.3. Sensitivity:

396 The sensitivity depends on the sputtering time, ionization, extraction of the Fe^+ ion
397 from the matrix and secondary ions transmission until the detectors. It is defined as count rate
398 per ppm of Fe in the analyzed phase per nA of the primary beam (cps/ppm/nA). As the Fe
399 content is constant in pyrites, the expression of the sensitivity is approximately proportional
400 to the ion yield:

$$401 \text{}^{56}\text{Fe yield} = \text{}^{56}\text{Fe}^+ / \text{P intensity.}$$

402 The sensitivity calculation is commonly used to evaluate the transmission of an ion
403 microprobe. **Table 1** shows the ^{56}Fe ion yields on Balmat pyrite, obtained over the different
404 sessions at CRPG-IPNT and SwissSIMS equipped with the Hyperion-II source. We
405 compared these results to the sensitivity obtained with the conventional Duoplasmatron
406 source^{45,46}. The sensitivities determined on Balmat pyrite range from 1.56×10^7 to
407 2.01×10^7 cps/nA at CRPG-IPNT. Sessions performed at SwissSIMS (July 2019, January
408 2020, March 2020 and September 2020) show similar sensitivities, ranging from
409 1.49×10^7 cps/nA to 1.61×10^7 cps/nA. Higher sensitivities obtained at CRPG-IPNT compared
410 to SwissSIMS are explained by different widths of the entrance slit. Sensitivities obtained
411 with the Duoplasmatron source vary from 1.2×10^7 cps/nA⁴⁵ to 1.5×10^7 cps/nA⁴⁶. However, the
412 resulting transmissions in the two Duoplasmatron-based studies are not directly comparable
413 as the width of the field aperture (FA), the entrance and exit slit and the Maximum Area
414 (MA) are different between these two studies (**Table 1**). In order to compare sensitivities
415 obtained by Hyperion and Duoplasmatron, we performed two tests using (1) a MA 80 and
416 field aperture closed at $\sim 2500 \mu\text{m}$ (comparable with sensitivity obtained previously⁴⁵) and (2)
417 a MA 160 and an opened field aperture to transmit 100% of the signal⁴⁶. Using a MA of 80
418 and similar FA, entrance and exit slit widths, the ^{56}Fe sensitivity is 1.56×10^7 cps/nA and better
419 than the 1.2×10^7 cps/nA obtained with the Duoplasmatron⁴⁵. The higher sensitivity with the
420 Hyperion is due to the use of a smaller beam, which is less clipped in the field aperture
421 compared to the Duoplasmatron beam. Using a MA 160, we obtained a sensitivity of
422 5.05×10^6 cps/nA, which is lower than the 1.5×10^7 cps/nA achieved by the Duoplasmatron⁴⁶.
423 However, these sensitivities are not directly comparable as O_2^- and O^- primary beams were
424 respectively used in Whitehouse and Fedo⁴⁶ and in the present study. The higher sensitivity
425 obtained previously⁴⁶ can be thus attributed to the more efficient sputtering rate of the O_2^-

426 beam. The use of smaller primary beam currents reduces the size of the crossover and off-
427 axis aberrations of the secondary ion beam, which helps to define a sharper slit image.
428 Therefore, for a given MRP, the entrance slit can be more opened using the Hyperion and this
429 results in a gain of sensitivity compared to the Duoplasmatron. This test illustrates the ability
430 of the source to provide enough secondary ion signals with a 3nA beam focused on a 3 μ m
431 spot and to achieve a better sensitivity than that delivered by Duoplasmatron. The Fe
432 secondary ion signals produced by the 3nA primary beam can be detected by MCFC and
433 thus, provides high precision $\delta^{56}\text{Fe}$ measurements along with higher spatial resolution.

434

435 *3.4. Reproducibility and accuracy:*

436 The reproducibility of the $\delta^{56}\text{Fe}$ measurements on the Balmat reference material was
437 established over three sessions (February 2018, April 2018 and September 2020) at CRPG-
438 IPNT and four sessions (July 2019, January 2020, March 2020 and June 2020) at SwissSIMS
439 Lausanne (**Table 2**). Balmat pyrite (same grain) displays a respective long-term
440 reproducibility of $\pm 0.25\%$ (2SD) for 166 measurements (**Figure 6**) at CRPG-IPNT and
441 $\pm 0.22\%$ (2SD) for 185 measurements (June 2020) at SwissSIMS ion probe. The short-term
442 reproducibility on Balmat pyrite varied from $\pm 0.24\%$ (2SD, February 2018, n=33, **Table S3**
443 **supporting information B**) to $\pm 0.26\%$ (2SD, April 2018, n=133) at CRPG-IPNT and from
444 $\pm 0.18\%$ (2SD, March 2020, n=33) to $\pm 0.35\%$ (2SD, January 2020, n=16) at SwissSIMS. The
445 reproducibility obtained on SpainCR standard (July 2018) is close to those measured in
446 Balmat pyrite with a value of $\pm 0.28\%$ (2SD, n=61). Published data obtained using the ^{16}O -
447 Duoplasmatron source⁶⁸ on three days of analysis show a reproducibility of $\pm 0.44\%$ (2SD,
448 n=17) on the same grain of Balmat, which highlight the better stability of the Hyperion-II
449 source compared to the Duoplasmatron.

450 The accuracy of the SIMS technique was tested on two pyrite standards which have
451 different isotopic compositions. We used Balmat as a reference standard and considered
452 SpainCR as an unknown pyrite. The $\delta^{56}\text{Fe}$ value for SpainCR was determined using the IMF
453 calculated on Balmat reference material. The $\delta^{56}\text{Fe}$ value for SpainCR pyrite calculated at
454 $+0.64 \pm 0.26\%$ (2SD, n=2) is in quite good agreement with the value of $\delta^{56}\text{Fe} = +0.52 \pm 0.03\%$
455 determined by MC-ICP-MS, demonstrating the accuracy of the SIMS method.

456

457

458

4. Conclusions

An ion microprobe equipped with the new Hyperion-II Radio Frequency source is able to determine iron isotope ratios with high accuracy, at high precision ($\sim 0.25\%$, 2SD) and high spatial resolution ($3\mu\text{m}$). We have detailed a procedure to achieve $\delta^{56}\text{Fe}$ measurements a primary intensity 3 times lower than that traditionally delivered by the Duoplasmatron source, yet we achieved better precision. The MRP was intentionally set at a lower value than that required to resolve $^{56}\text{FeH}^+$ from $^{57}\text{Fe}^+$ to attain a minimum $^{56}\text{Fe}^+$ count rate of 4×10^7 cps on a pyrite reference material to produce high precision $\delta^{56}\text{Fe}$ values. The level of $^{56}\text{FeH}^+$ is low compared to the intensity of $^{57}\text{Fe}^+$ under high vacuum. A MRP of ~ 6700 is sufficient to limit its contribution to ^{57}Fe signal. In our sample set, we demonstrated the absence of topography and crystal orientation effects. Currently, this new procedure is applied to major iron-bearing minerals to better constrain natural iron isotopic variabilities at micrometric scale in sedimentary pyrites. The future investigation of *in situ* $\delta^{56}\text{Fe}$ signatures in minor iron-bearing phases such as oxides, carbonates and silicates will serve as a promising tool to answer fundamental questions in extraterrestrial and terrestrial petrology and to gain a better understanding of the biogeochemical iron cycles.

Acknowledgements:

We thank Caroline de Meyer for assistance with the EBSE analysis. We thank Claire Rollion-Bard for providing SpainCR pyrite standard, Katharina Marger for her help with the EPMA analysis, and Damien Cividini (CRPG) for help in MC-ICP-MS measurements. We thank David Zakharov for fruitful discussions that led to the improvement of the manuscript. We appreciated constructive reviews from Cees-Jan De Hoog and three anonymous reviewers. This research was supported by the European Union's Horizon H2020 research and innovation program ERC (STROMATA, grant agreement 759289; PI Johanna Marin-Carbonne).

495 **References:**

496

497 1. Beard BL, Johnson CM. High precision iron isotope measurements of terrestrial and
498 lunar materials. *Geochim Cosmochim Acta*. 1999;63(11-12):1653-1660.
499 [https://doi.org/10.1016/S0016-7037\(99\)00089-7](https://doi.org/10.1016/S0016-7037(99)00089-7).

500 2. Anbar AD, Roe JE, Barling J, Neelson KH. Nonbiological fractionation of iron
501 isotopes. *Science*. 2000;288(5463):126-128. doi: 10.1126/science.288.5463.126.

502 3. Dauphas N, Janney PE, Mendybaev RA, et al. Chromatographic separation and
503 multicollection-ICPMS analysis of iron. Investigating mass-dependent and-
504 independent isotope effects. *Anal Chem*. 2004;76(19):5855-5863.
505 <https://doi.org/10.1021/ac0497095>.

506 4. Berglund M, Wieser ME. Isotopic compositions of the elements 2009 (IUPAC
507 Technical Report). *Pure Applied Chem*. 2011;83(2):397-410.
508 <https://doi.org/10.1351/PAC-REP-10-06-02>.

509 5. Craddock PR, Dauphas N. Iron isotopic compositions of geological reference
510 materials and chondrites. *Geostand Geoanal Res*. 2011;35(1):101-123.
511 <https://doi.org/10.1111/j.1751-908X.2010.00085.x>.

512 6. Taylor PDP, Maeck R and De Bièvre P. Determination of the absolute isotopic
513 composition and atomic weight of a reference sample of natural iron. *Int J Mass Spect*
514 *Ion Proc*. 1992; 121(1-2), 111-125.

515 7. Mullane E, Russell SS, Gounelle M. Nebular and asteroidal modification of the iron
516 isotope composition of chondritic components. *Earth Planet Sci Lett*. 2005;239(3-
517 4):203-218. <https://doi.org/10.1016/j.epsl.2005.07.026>.

518 8. Poitrasson F, Freydier R. Heavy iron isotope composition of granites determined by
519 high resolution MC-ICP-MS. *Chem Geol*. 2005;222(1-2):132-147.
520 <https://doi.org/10.1016/j.chemgeo.2005.07.005>.

521 9. Needham AW, Porcelli D, Russell SS. An Fe isotope study of ordinary
522 chondrites. *Geochim Cosmochim Acta*. 2009;73(24):7399-7413.
523 <https://doi.org/10.1016/j.gca.2009.08.034>.

524 10. Hezel DC, Needham AW, Armytage R, et al. A nebula setting as the origin for bulk
525 chondrule Fe isotope variations in CV chondrites. *Earth Planet Sci Lett*. 2010;296(3-
526 4):423-433. <https://doi.org/10.1016/j.epsl.2010.05.029>.

527 11. Dauphas N, John SG, Rouxel OJ. Iron isotope systematics. *Rev Mineral Geochem*.
528 2017;82(1):415-510. <https://doi.org/10.2138/rmg.2017.82.11>.

529 12. Rouxel OJ, Bekker A, Edwards KJ. Iron isotope constraints on the Archean and
530 Paleoproterozoic ocean redox state. *Science*. 2005;307(5712):1088-1091. doi:
531 10.1126/science.1105692.

532 13. Johnson CM, Beard BL, Roden EE. The iron isotope fingerprints of redox and
533 biogeochemical cycling in modern and ancient Earth. *Annu Rev Earth Planet Sci*.
534 2008;36:457-493. doi:10.1146/annurev.earth.36.031207.124139.

535 14. Severmann S, Lyons TW, Anbar A, McManus J, Gordon G. Modern iron isotope
536 perspective on the benthic iron shuttle and the redox evolution of ancient
537 oceans. *Geology*. 2008;36(6):487-490. <https://doi.org/10.1130/G24670A.1>.

- 538 15. Czaja AD, Johnson CM, Beard BL, Eigenbrode JL, Freeman KH, Yamaguchi KE.
539 Iron and carbon isotope evidence for ecosystem and environmental diversity in the~
540 2.7 to 2.5 Ga Hamersley Province, Western Australia. *Earth Planet Sci Lett.*
541 2010;292(1-2):170-180. <https://doi.org/10.1016/j.epsl.2010.01.032>
- 542 16. Marin-Carbonne J, Rollion-Bard C, Bekker A, et al. Coupled Fe and S isotope
543 variations in pyrite nodules from Archean shale. *Earth Planet Sci Lett.* 2014;392:67-
544 79. <https://doi.org/10.1016/j.epsl.2014.02.009>.
- 545 17. Johnson C, Beard B, Weyer S. Iron Geochemistry: An Isotopic Perspective. 2020;
546 Springer, Cham.
- 547 18. Johnson CM, Beard B, Roden EE, Newman DK, Nealon KH. Isotopic constraints on
548 biogeochemical cycling of Fe. *Rev Mineral Geochem.* 2004; 55, 359-408.
549 <https://doi.org/10.2138/gsrmg.55.1.359>
- 550 19. Lovley DR, Stolz JF, Nord GL, Phillips EJ. Anaerobic production of magnetite by a
551 dissimilatory iron-reducing microorganism. *Nature.* 1987; 330, 252-254.
- 552 20. Bullen TD and McMahon PM. Using stable Fe isotopes to assess microbially-
553 mediated Fe³⁺ reduction in a jet-fuel contaminated aquifer. *Mineral Mag.*
554 1998;62:255-256.
- 555 21. Beard BL, Johnson CM, Cox L, Sun H, Nealon KH, Aguilar C. Iron isotope
556 biosignatures. *Science.* 1999;285(5435):1889-1892. doi:
557 10.1126/science.285.5435.1889.
- 558 22. Crosby HA, Johnson CM, Roden EE, Beard BL. Coupled Fe (II)– Fe (III) electron
559 and atom exchange as a mechanism for Fe isotope fractionation during dissimilatory
560 iron oxide reduction. *Env Sci Technol.* 2005;39(17):6698-6704.
561 <https://doi.org/10.1021/es0505346>.
- 562 23. Crosby HA, Roden EE, Johnson CM, Beard BL. The mechanisms of iron isotope
563 fractionation produced during dissimilatory Fe (III) reduction by *Shewanella*
564 *putrefaciens* and *Geobacter sulfurreducens*. *Geobiology.* 2007;5(2):169-
565 189. <https://doi.org/10.1111/j.1472-4669.2007.00103.x>.
- 566 24. Percak-Dennett EM, Beard BL, Xu H, Konishi H, Johnson CM, Roden EE. Iron
567 isotope fractionation during microbial dissimilatory iron oxide reduction in simulated
568 Archaean seawater. *Geobiology.* 2011;9(3):205-220. <https://doi.org/10.1111/j.1472-4669.2011.00277.x>.
- 570 25. Johnson CM, Skulan JL, Beard BL, Sun H, Nealon KH, Braterman PS. Isotopic
571 fractionation between Fe (III) and Fe (II) in aqueous solutions. *Earth Planet Sci Lett.*
572 2002;195(1-2):141-153. [https://doi.org/10.1016/S0012-821X\(01\)00581-7](https://doi.org/10.1016/S0012-821X(01)00581-7).
- 573 26. Welch SA, Beard BL, Johnson CM, Braterman PS. Kinetic and equilibrium Fe
574 isotope fractionation between aqueous Fe (II) and Fe (III). *Geochim Cosmochim Acta.*
575 2003;67(22):4231-4250. [https://doi.org/10.1016/S0016-7037\(03\)00266-7](https://doi.org/10.1016/S0016-7037(03)00266-7).
- 576 27. Skulan JL, Beard BL, Johnson CM. Kinetic and equilibrium Fe isotope fractionation
577 between aqueous Fe (III) and hematite. *Geochim Cosmochim Acta.*
578 2002;66(17):2995-3015. [https://doi.org/10.1016/S0016-7037\(02\)00902-X](https://doi.org/10.1016/S0016-7037(02)00902-X).
- 579 28. Beard BL, Handler RM, Scherer MM, et al. Iron isotope fractionation between
580 aqueous ferrous iron and goethite. *Earth Planet Sci Lett.* 2010;295(1-2):241-250.
581 <https://doi.org/10.1016/j.epsl.2010.04.006>.

- 582 29. Wu L, Beard BL, Roden EE, Kennedy CB, Johnson CM. Stable Fe isotope
583 fractionations produced by aqueous Fe (II)-hematite surface interactions. *Geochim*
584 *Cosmochim Acta*. 2010;74(15):4249-4265. <https://doi.org/10.1016/j.gca.2010.04.060>.
- 585 30. Wu L, Beard BL, Roden EE, Johnson CM. Stable iron isotope fractionation between
586 aqueous Fe (II) and hydrous ferric oxide. *Env Sci Technol*. 2011;45(5):1847-1852.
587 <https://doi.org/10.1021/es103171x>.
- 588 31. Frierdich AJ, Nebel O, Beard BL, Johnson CM. Iron isotope exchange and
589 fractionation between hematite (α -Fe₂O₃) and aqueous Fe (II): A combined three-
590 isotope and reversal-approach to equilibrium study. *Geochim Cosmochim Acta*.
591 2019;245:207-221. <https://doi.org/10.1016/j.gca.2018.10.033>.
- 592 32. Croal LR, Johnson CM, Beard BL, Newman DK. Iron isotope fractionation by Fe
593 (II)-oxidizing photoautotrophic bacteria. *Geochim Cosmochim Acta*.
594 2004;68(6):1227-1242. <https://doi.org/10.1016/j.gca.2003.09.011>.
- 595 33. Bullen TD, White AF, Childs CW, Vivit DV, Schulz MS. Demonstration of
596 significant abiotic iron isotope fractionation in nature. *Geology*. 2001;29(8):699-702.
597 [https://doi.org/10.1130/0091-7613\(2001\)029<0699:DOSAII>2.0.CO;2](https://doi.org/10.1130/0091-7613(2001)029<0699:DOSAII>2.0.CO;2).
- 598 34. Beard BL and Johnson CM. Fe isotope variations in the modern and ancient earth and
599 other planetary bodies. *Rev Mineral Geochem*. 2004;55(1):319-357.
600 <https://doi.org/10.2138/gsrmg.55.1.319>.
- 601 35. Rickard D, Grimes S, Butler I, Oldroyd A and Davies KL. Botanical constraints on
602 pyrite formation. *Chem. Geol*. 2007;236, 228-246.
603 <https://doi.org/10.1016/j.chemgeo.2006.09.011>.
- 604 36. Luther III GW. Pyrite synthesis via polysulfide compounds. *Geochim Cosmochim*
605 *Acta*. 1991;55, 2839-2849. [https://doi.org/10.1016/0016-7037\(91\)90449-F](https://doi.org/10.1016/0016-7037(91)90449-F).
- 606 37. Rickard D. *Sulfidic sediments and sedimentary rocks*. Newnes. 2017.
- 607 38. Rickard D. Sedimentary pyrite framboid size-frequency distributions: A meta-
608 analysis. *Palaeogeog palaeoclim palaeoeco*. 2019.
609 <https://doi.org/10.1016/j.palaeo.2019.03.010>.
- 610 39. Yoshiya K, Nishizawa M, Sawaki Y, et al. In situ iron isotope analyses of pyrite and
611 organic carbon isotope ratios in the Fortescue Group: Metabolic variations of a Late
612 Archean ecosystem. *Precambrian Res*. 2012;212:169-193.
613 <https://doi.org/10.1016/j.precamres.2012.05.003>.
- 614 40. Nishizawa M, Yamamoto H, Ueno Y, et al. Grain-scale iron isotopic distribution of
615 pyrite from Precambrian shallow marine carbonate revealed by a femtosecond laser
616 ablation multicollector ICP-MS technique: possible proxy for the redox state of
617 ancient seawater. *Geochim Cosmochim Acta*. 2010;74(9):2760-2778.
618 <https://doi.org/10.1016/j.gca.2010.02.014>.
- 619 41. Liu MC, McKeegan KD, Harrison TM, Jarzebinski G, Vltava L. The Hyperion-II
620 radio-frequency oxygen ion source on the UCLA ims1290 ion microprobe: Beam
621 characterization and applications in geochemistry and cosmochemistry. *Int J Mass*
622 *Spectrom*. 2018;424:1-9. <https://doi.org/10.1016/j.ijms.2017.11.007>.
- 623

- 624 42. Fukuda K, Beard BL, Dunlap DR, et al. Magnesium isotope analysis of olivine and
625 pyroxene by SIMS: Evaluation of matrix effects. *Chem Geol.* 2020;119482.
626 <https://doi.org/10.1016/j.chemgeo.2020.119482>.
- 627 43. Villeneuve J, Chaussidon M, Marrocchi Y, Deng Z, Watson EB. High-precision in
628 situ silicon isotopic analyses by multi-collector secondary ion mass spectrometry in
629 olivine and low-calcium pyroxene. *Rapid Commun Mass Spectrom.*
630 2019;33(20):1589-1597. <https://doi.org/10.1002/rcm.8508>.
- 631 44. Ushikubo T, Nakashima D, Kimura M, Tenner TJ, Kita NT. Contemporaneous
632 formation of chondrules in distinct oxygen isotope reservoirs. *Geochim Cosmochim*
633 *Acta.* 2013;109, 280-295. <https://doi.org/10.1016/j.gca.2013.01.045>.
- 634 45. Marin-Carbonne J, Rollion-Bard C, Luais B. In-situ measurements of iron isotopes by
635 SIMS: MC-ICP-MS intercalibration and application to a magnetite crystal from the
636 Gunflint chert. *Chem Geol.* 2011;285(14):50-61.
637 <https://doi.org/10.1016/j.chemgeo.2011.02.019>.
- 638 46. Whitehouse MJ, Fedo CM. Microscale heterogeneity of Fe isotopes in > 3.71 Ga
639 banded iron formation from the Isua Greenstone Belt, southwest Greenland. *Geology.*
640 2007;35(8):719-722. <https://doi.org/10.1130/G23582A.1>.
- 641 47. Muller É, Philippot P, Rollion-Bard C, Cartigny P, Assayag N, Marin-Carbonne J,
642 Mohan MR and Sarma DS. Primary sulfur isotope signatures preserved in high-grade
643 Archean barite deposits of the Sargur Group, Dharwar Craton, India. *Precambrian*
644 *Res.* 2017; 295, 38-47. <https://doi.org/10.1016/j.precamres.2017.04.029>.
- 645 48. Muller É, Philippot P, Rollion-Bard C and Cartigny P. Multiple sulfur-isotope
646 signatures in Archean sulfates and their implications for the chemistry and dynamics
647 of the early atmosphere. *Proc Nat Ac Sci.* 2016; 113(27), 7432-7437.
648 <https://doi.org/10.1073/pnas.1520522113>.
- 649 49. El Korh A, Luais B, Deloule E, Cividini D. Iron isotope fractionation in subduction-
650 related high-pressure metabasites (Ile de Groix, France). *Contributions to Mineralogy*
651 *and Petrology.* 2017;172(6):41. doi: 10.1007/s00410-017-1357-x.
- 652 50. Liu PP, Zhou MF, Luais B, Cividini D, Rollion-Bard C. Disequilibrium Fe isotope
653 fractionation during the high-temperature magmatic differentiation of the Baima Fe-
654 Ti oxide-bearing mafic intrusion, SW China. *Earth Planet Sci Lett.* 2014; 339, 21-29.
655 <https://doi.org/10.1016/j.epsl.2014.05.002>
- 656 51. Kita NT, Ushikubo T, Fu B, Valley JW. High precision SIMS oxygen isotope analysis
657 and the effect of sample topography. *Chem Geol.* 2009;264(1-4):43-57.
658 <https://doi.org/10.1016/j.chemgeo.2009.02.012>.
- 659 52. Bayliss P. Crystal structure refinement of a weakly anisotropic pyrite. *Am Mine.*
660 1977 ; 62(11-12), 1168-1172.
- 661 53. Prior DJ, Boyle AP, Brenker F, Cheadle MC, Day A, Lopez G, Peruzzo L, Potts GJ,
662 Reddy S, Spiess R, Timms NE, Trimby P, Wheeler J and Zetterström L. The
663 application of electron backscatter diffraction and orientation contrast imaging in the
664 SEM to textural problems in rocks. *Am Mine.* 1999; 84, 1741-1759.
665 <https://doi.org/10.2138/am-1999-11-1204>.
- 666 54. Shimizu N, Hart SR. Applications of the ion microprobe to geochemistry and
667 cosmochemistry. *Annu Rev Earth Planet Sci.* 1982;10(1):483-526.

- 668 55. Eiler JM, Graham C, Valley JW. SIMS analysis of oxygen isotopes: Matrix effects in
669 complex minerals and glasses. *Chem Geol.* 1997;138(3-4):221-244.
- 670 56. Chaussidon M., Albarede F, Sheppard SMF. Sulphur isotope heterogeneity in the
671 mantle from ion microprobe measurements of sulphide inclusions in
672 diamonds. *Nature.* 1987;330(6145):242-244.
- 673 57. Kita NT, Huberty JM, Kozdon R, Beard BL, Valley JW. High-precision SIMS
674 oxygen, sulfur and iron stable isotope analyses of geological materials: Accuracy,
675 surface topography and crystal orientation. *Surf Interface Anal.* 2011;43(1-2):427-
676 431. <https://doi.org/10.1002/sia.3424>.
- 677 58. Vielzeuf D, Champenois M, Valley JW, Brunet F, Devidal JL. SIMS analyses of
678 oxygen isotopes: matrix effects in Fe–Mg–Ca garnets. *Chem Geol.* 2005;223(4):208-
679 226. <https://doi.org/10.1016/j.chemgeo.2005.07.008>.
- 680 59. Vho A, Rubatto D, Putlitz B, Bouvier AS. New Reference Materials and Assessment
681 of Matrix Effects for SIMS Measurements of Oxygen Isotopes in Garnet. *Geostand*
682 *Geoanal Res.* 2020. <https://doi.org/10.1111/ggr.12324>.
- 683 60. Deloule E, Chaussidon M, Allé P. Instrumental limitations for isotope measurements
684 with a Caméca® IMS-3f ion microprobe: Example of H, B, S and Sr. *Chem Geol Isot*
685 *Geosci Sect.* 1992;101(1–2):187-192.
- 686 61. Crossley RJ, Evans KA, Jeon H, Kilburn MR. Insights into sulfur cycling at
687 subduction zones from in-situ isotopic analysis of sulfides in high-pressure
688 serpentinites and ‘hybrid’ samples from Alpine Corsica. *Chem Geol.* 2018; 493, 359-
689 378. <https://doi.org/10.1016/j.chemgeo.2018.06.014>.
- 690 62. Chaussidon M, Deng Z, Villeneuve J, et al. In situ analysis of non- traditional
691 isotopes by SIMS and LA–MC–ICP–MS: Key aspects and the example of Mg
692 isotopes in olivines and silicate glasses. *Rev Mineral Geochem.* 2017;82(1):127-163.
693 <https://doi.org/10.2138/rmg.2017.82.5>.
- 694 63. Kozdon R, Kita NT, Huberty JM, Fournelle JH, Johnson CA, Valley JW. In situ
695 sulfur isotope analysis of sulfide minerals by SIMS: Precision and accuracy, with
696 application to thermometry of ~ 3.5 Ga Pilbara cherts. *Chem Geol.* 2010;275(3-
697 4):243-253. <https://doi.org/10.1016/j.chemgeo.2010.05.015>.
- 698 64. Wingate MTD, Compston W. Crystal orientation effects during ion microprobe U–Pb
699 analysis of baddeleyite. *Chem Geol.* 2000;168(1-2):75-97.
700 [https://doi.org/10.1016/S0009-2541\(00\)00184-4](https://doi.org/10.1016/S0009-2541(00)00184-4).
- 701 65. LaFlamme C, Martin L, Jeon H, Reddy SM, Selvaraja V, Caruso S, Bui TH, Roberts
702 MP, Voute F, Hagemann S, Wacey D, Littman S, Wing B, Fiorentini M and Kilburn
703 MR. In situ multiple sulfur isotope analysis by SIMS of pyrite, chalcopyrite,
704 pyrrhotite, and pentlandite to refine magmatic ore genetic models. *Chem Geol.*
705 2016; 444, 1-15. <https://doi.org/10.1016/j.chemgeo.2016.09.032>
- 706 66. Gnaser H. Energy and angular distributions of sputtered species. In: *Sputtering by*
707 *particle bombardment*. Springer, Berlin, Heidelberg. 2007;231-328.
- 708 67. Huberty JM, Kita NT, Kozdon R, et al. Crystal orientation effects in $\delta^{18}\text{O}$ for
709 magnetite and hematite by SIMS. *Chem Geol.* 2010;276(3-4):269-283.
710 <https://doi.org/10.1016/j.chemgeo.2010.06.012>.

711 68. Marin-Carbonne J, Busigny V, Miot J, et al. In Situ Fe and S isotope analyses in
712 pyrite from the 3.2 Ga Mendon Formation (Barberton Greenstone Belt, South Africa):
713 Evidence for early microbial iron reduction. *Geobiology*. 2020.
714 <https://doi.org/10.1111/gbi.12385>.
715

716

717

718

719

720

721

722

723

724

725

726

727

728

729

730

731

732

733

734

735

736

737

738

739

740

741

742

743

744

745

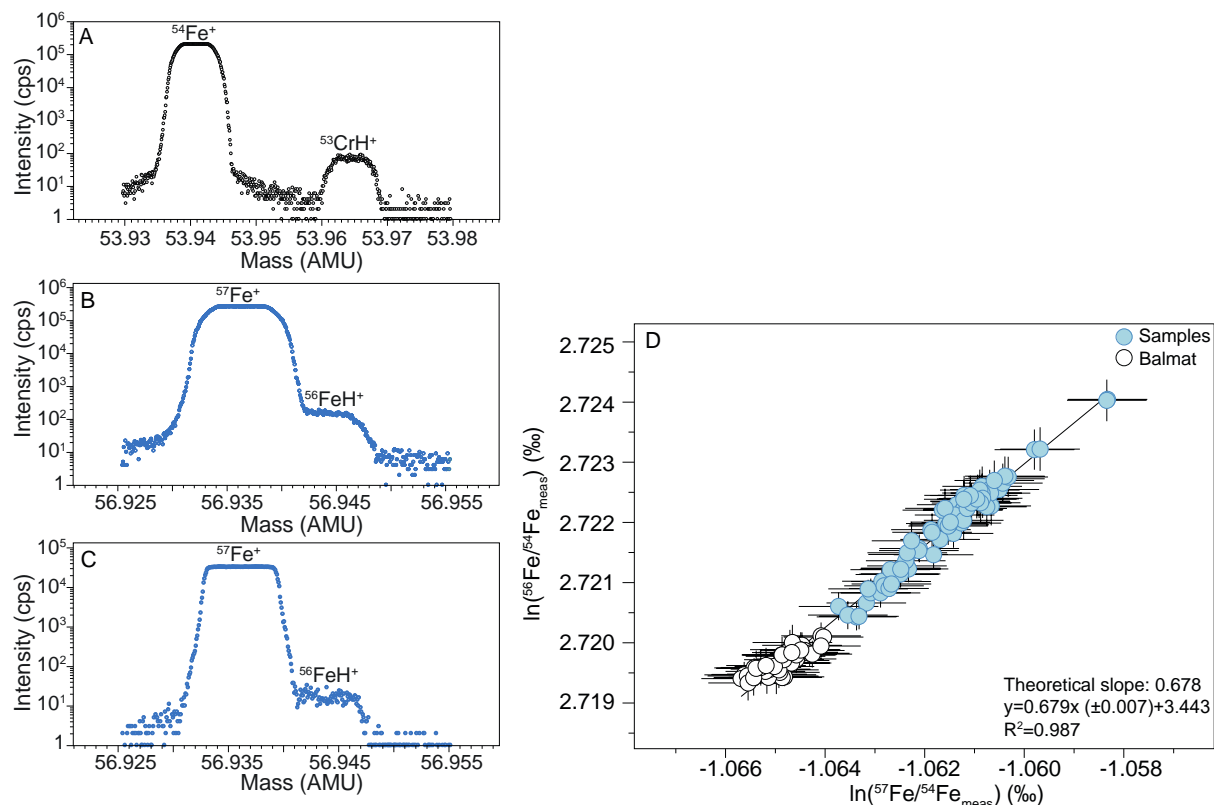
746 TABLE 1 SIMS settings for each Fe isotopes session at CRPG-IPNT (February 2018,
747 April 2018 and September 2020) and SwissSIMS (July 2019, January 2020, March 2020 and
748 June 2020) using the Hyperion-II source and resulting $^{56}\text{Fe}^+$ intensities and ion yields
749 measured on Balmat pyrite. Comparison with settings and $^{56}\text{Fe}^+$ yields measured with the
750 Duoplasmatron^{45,46}.

THIS STUDY								PUBLISHED DATA	
CRPG-IPNT				SwissSIMS				CRPG-IPNT	NordSIMS
Hyperion-II				Hyperion-II				Duoplasmatron	
Session	Feb.18	Ap.18	Sep.20	Jul.19	Jan.20	Mar.20	Jun.20	Ref. 45	Ref.46
Field Ap. (μm)	2000		2400	2000				2500	3000
Contrast Ap. (μm)	400			400				400	
Max. Area	80		80 <i>160</i>	80				80	160
Entrance Slit (μm)	85		61	61				-	60
Energy slit (eV)	50			50				50	60
Slit Mode	Circular			Circular				Circular	
Exit slit	150 μm (slit 3)			150 μm (slit 3)				150 μm (slit 3)	250 μm (slit 2)
MRP	6100		6800	6700-6800				~7000	<6000
Primary Intensity (nA)	3.40	3.70	3.00	3.14	3.05	2.99	2.80	10	10
$^{56}\text{Fe}^+$ count rate on Balmat (cps)	6.5E+7	7.45E+7	4.70E+7 <i>1.51E+7</i>	4.90E+7	4.85E+7	4.46E+7	4.49E+7	~ 1.2E+8	~1.5E+8
$^{56}\text{Fe}^+$ yield on Balmat (cps/nA)	1.87E+7	2.01E+7	1.56E+7 <i>5.05E+6</i>	1.56E+7	1.59E+7	1.49E+7	1.61E+7	~1.2E+7	1.5E+7

751 TABLE 2 True $\delta^{56}\text{Fe}$ values of the standards (Balmat and SpainCR pyrites) and
 752 corresponding IMF during the different sessions at CRPG-IPNT and SwissSIMS and
 753 comparison with published IMF obtained with the Duoplasmatron⁴⁵. True $\delta^{56}\text{Fe}$ value of
 754 SpainCR standard was determined by MC-ICP-MS method at CRPG using a reported
 755 procedure⁵⁰. The reproducibility is reported as 2SD, standard deviation. n= number of
 756 analysis; *n.a*= not available data.
 757

INSTRUMENTAL MASS FRACTIONATION $\delta^{56}\text{Fe}_{\text{IMF}}$ AND REPRODUCIBILITY (2SD, ‰) (#ANALYSIS)									
CRPG-IPNT Hyperion-II					SwissSIMS Hyperion-II				CRPG- IPNT Duoplas matron
Session	Feb. 2018	Apr. 2018	Ju. 2018	Sept. 2020	Ju. 2019	Jan. 2020	Mar. 2020	Jun. 2020	ref.45
Balmat Py.	-33.10 ±0.24 (n=33)	-32.47 ±0.26 (n=133)	<i>n.a</i>	-31.20 ±0.30 (n=17)	-35.16 ±0.28 (n=41)	-27.23 ±0.35 (n=16)	-32.34 ±0.18 (n=33)	-33.06 ±0.22 (n=185)	-32.00 ±0.20
SpainCR Py.	<i>n.a</i>	<i>n.a</i>	-33.21 ±0.28 (n=68)	<i>n.a</i>	-35.50 ±0.32 (n=2)	<i>n.a</i>	<i>n.a</i>	<i>n.a</i>	<i>n.a</i>

758



759

760 **FIGURE 1** A) Scan of the ^{54}Fe signal on the axial EM, using a mass resolution of 6800 to reveal
 761 $^{53}\text{CrH}^+$ contribution. This scan was made on Russie magnetite standard which have a detectable Cr
 762 content. B) Scan of the ^{57}Fe signal on the axial EM, using a mass resolution of 6800 to reveal $^{56}\text{FeH}^+$
 763 contribution. C) High mass resolution (MRP 7800) scan of the ^{57}Fe signal, where $^{57}\text{Fe}^+$ and $^{56}\text{FeH}^+$
 764 peaks are separated. D) Three-isotope plot of the logarithm of the measured Fe isotope ratios in
 765 Balmat pyrite standard (white dots) and pyrites from sedimentary rocks (blue dots), corrected from
 766 the ^{54}Cr contribution (July 2020 session at SwissSIMS). The regression line gives a slope of
 767 0.679 ± 0.007 , which is in good agreement with the theoretical slope of 0.678 within the error bar. The
 768 theoretical value represents the mass dependent fractionation law for Fe isotopes using a simple
 769 harmonic oscillator approximation. Data are available in **Table S1 (supporting information B)**.

770

771

772

773

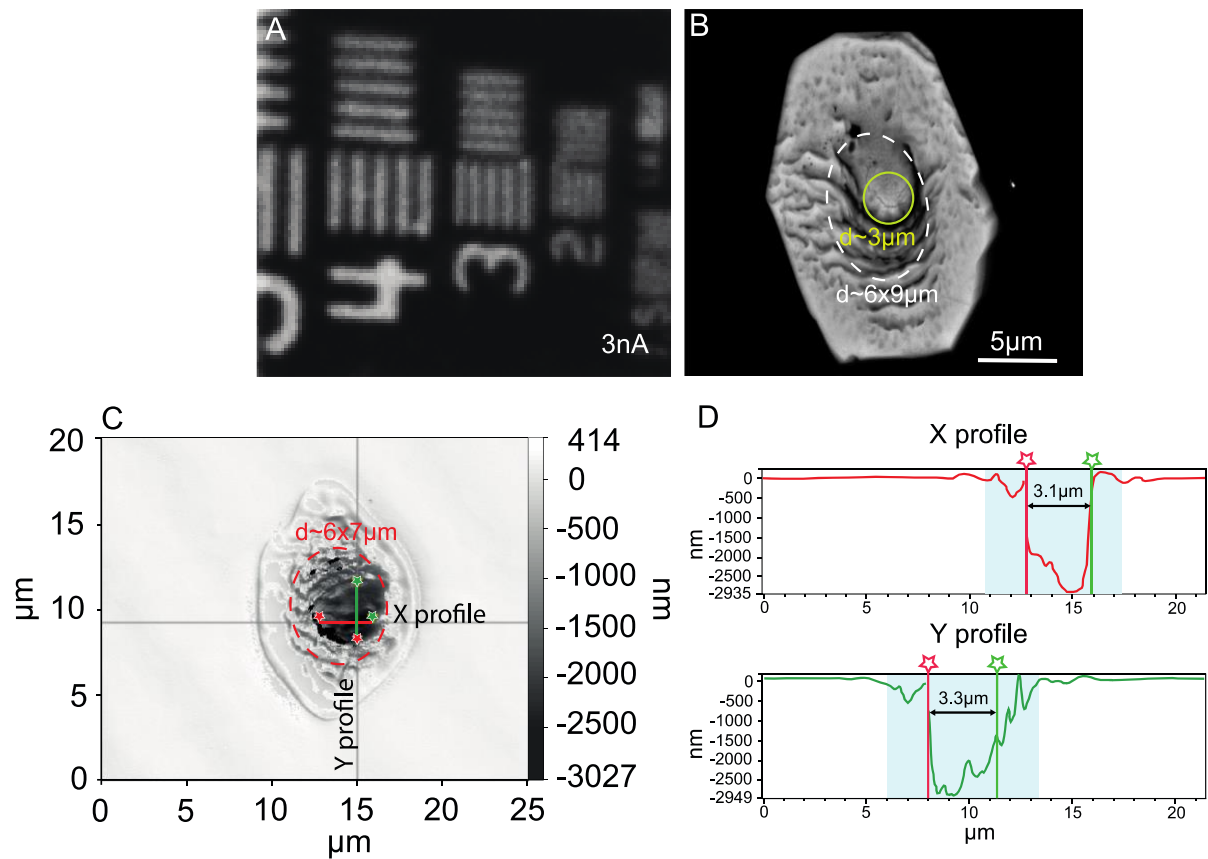
774

775

776

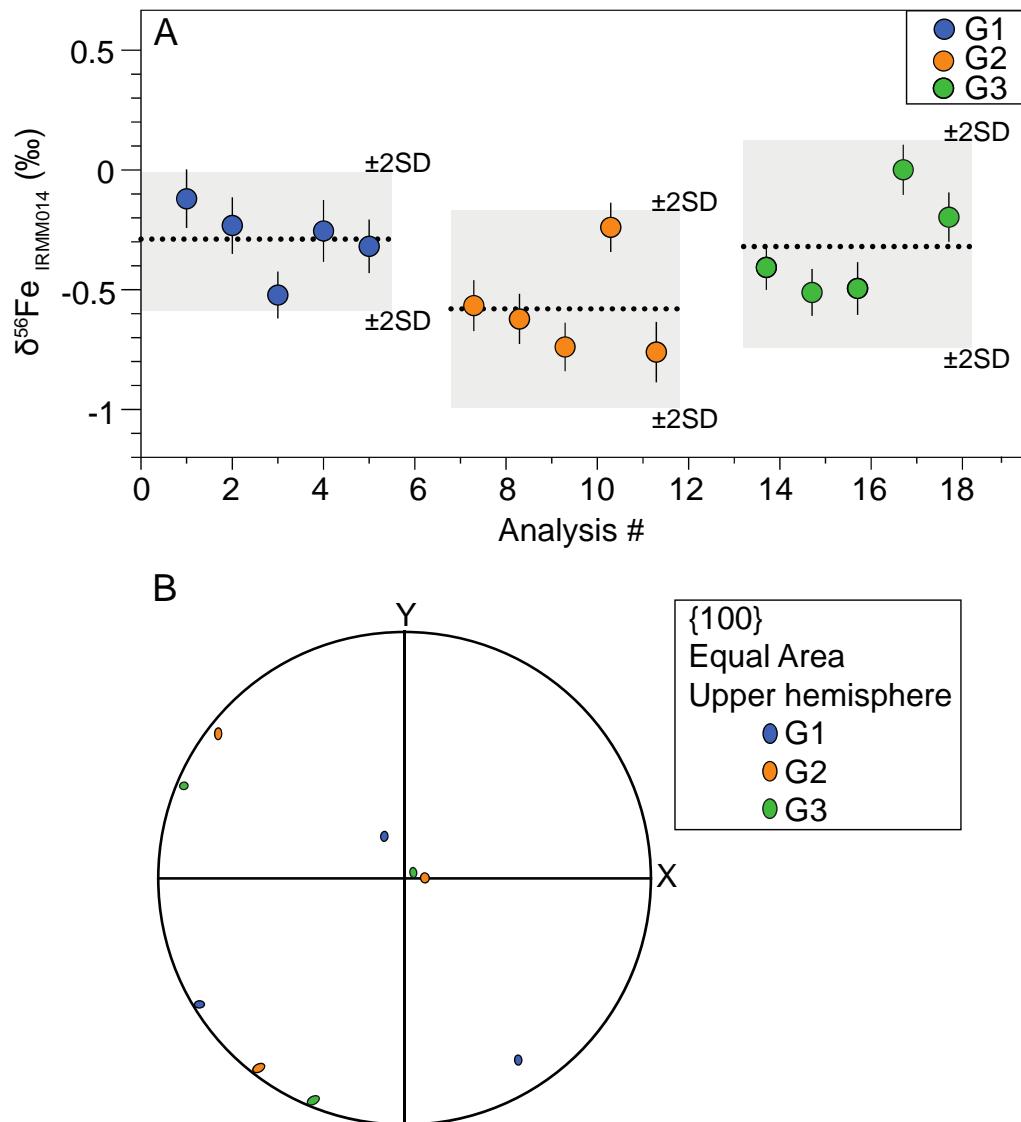
777

778



779

780 FIGURE 2 A) $^{30}\text{Si}^+$ image of the Si-grid on electron multiplier. The spatial resolution of
 781 the primary $^{16}\text{O}^-$ beam is determined according to the ability to differentiate two silicon bars
 782 on the $4\mu\text{m}$, $3\mu\text{m}$ or $2\mu\text{m}$ grid. B) SEM image of a sedimentary micro-pyrite after SIMS
 783 analyses. The shape of the spot is due to the position of the source which makes an angle with
 784 the sample surface. C) Image from interferometric microscope of the sputtering pit. D) X and
 785 Y topographic profiles measured by interferometric microscope. The profiles refer to the
 786 Figure 2C and show the diameter of the pit, which corresponds to the real spot size (measured
 787 at the bottom of the pit), and the sputtered area (blue area on Figure 2D and dashed red circle
 788 on **Figure 2C**, measured at the top of the pit).



789

790 FIGURE 3 Crystal orientation (September 2020) tests in Balmat pyrite standard. A) $\delta^{56}\text{Fe}$
 791 corrected from instrumental fractionation measured in three grains prepared in an indium
 792 mount. The reproducibility is given at 2SD and show no clear difference between the grains.
 793 Data are available in **Table S2 (supporting information)**. B) Upper hemisphere equal area
 794 (i.e. with Z pointing to the reader) EBSD pole figure showing the averaged crystallographic
 795 orientations of {100} for the three pyrite grains of interest. Note the strong clustering of [100]
 796 axes close to Z.

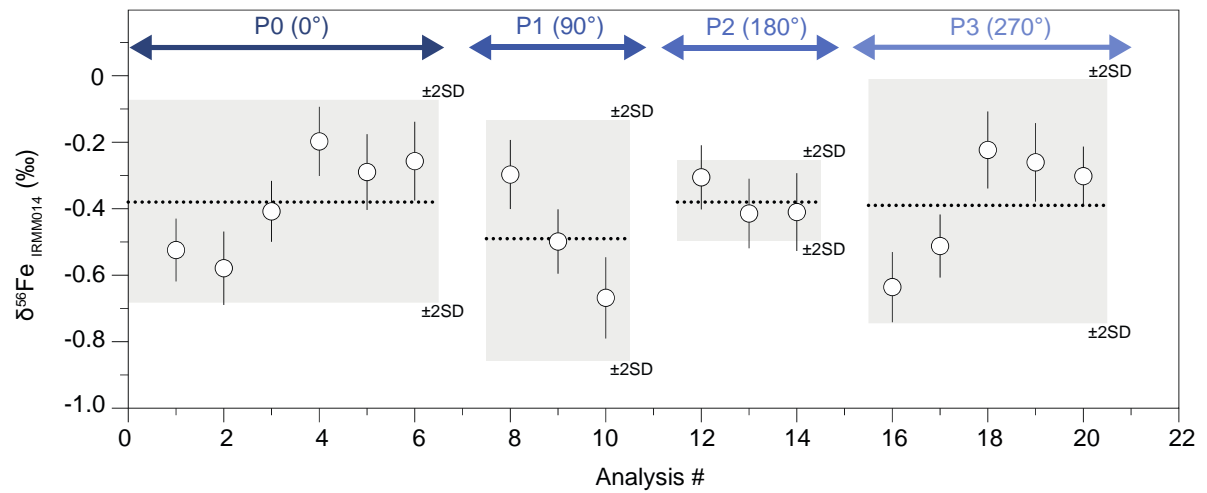
797

798

799

800

801



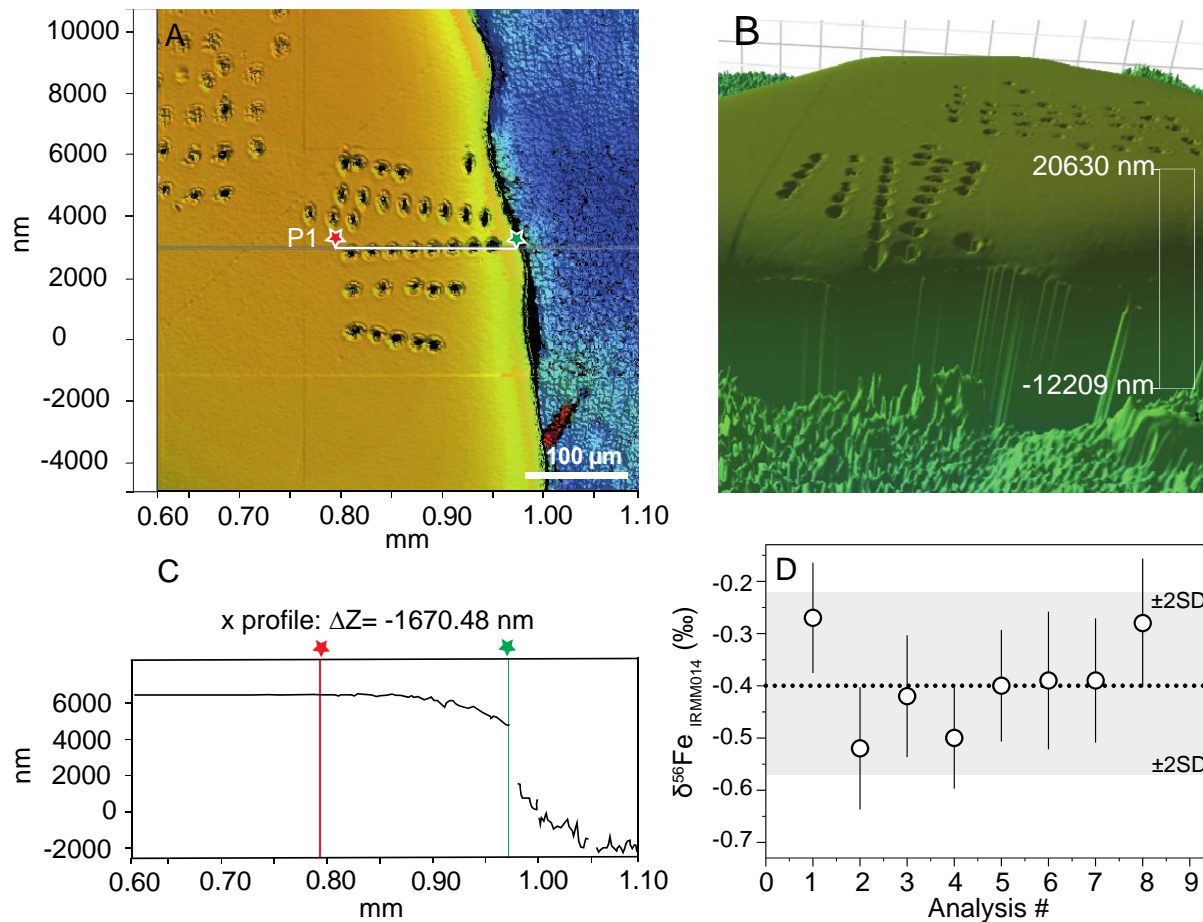
802

803 FIGURE 4 $\delta^{56}\text{Fe}$ values IMF-corrected of Balmat pyrite standard rotated by 90° (P1),
 804 180° (P2) and 270° (P3) compared to the initial position (P0). The external reproducibility is
 805 $\pm 0.30\text{‰}$ (2SD) and the internal variability are $\pm 0.10\text{‰}$ to $\pm 0.20\text{‰}$ (2SE), allowing to rule out
 806 orientation (channeling) effect on IMF variations. Data are available in **Table S2**
 807 (**supporting information**).

808

809

810



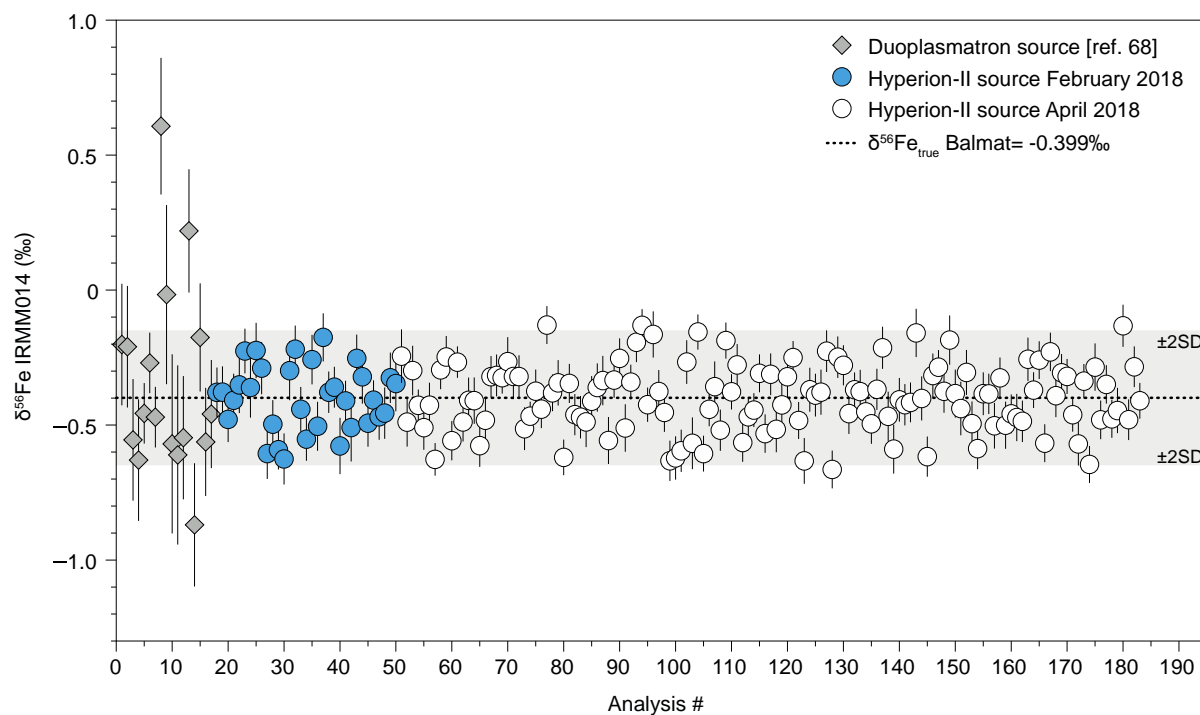
811

812 FIGURE 5 Profiles in Balmat reference material. A) Interferometric microscope image
 813 showing Pf1 profile in the pyrite grain. B) Interferometric microscope 3D image of the pyrite
 814 standard. C) Topographic profile following Pf1 transect. This profile shows a topographic
 815 difference of $\sim 1.5\mu\text{m}$ between the core (red star) and the rim (green star) of the grain. The
 816 gap after the green star ($\sim 7\mu\text{m}$) highlights the boundary between the pyrite grain and the
 817 indium. D) $\delta^{56}\text{Fe}$ values IMF-corrected in a core to rim profile performed in Balmat pyrite
 818 standard. Dashed black line is the true $\delta^{56}\text{Fe}$ value of Balmat standard ($\delta^{56}\text{Fe} = -0.399\text{‰}$). The
 819 uncertainty on average is $\pm 0.09\text{‰}$ (2SE) and the external reproducibility is $\pm 0.18\text{‰}$ (2SD,
 820 grey area). Data are available in **Table S2 (supporting information)**.

821

822

823



824

825

826 FIGURE 6 Long term reproducibility on Balmat pyrite reference material (0.25‰, 2SD).

827 Dots are $\delta^{56}\text{Fe}$ measured with Hyperion-II Radio-Frequency plasma source in February 2018

828 (blue dots) and April 2018 (white dots) session. Grey diamonds are $\delta^{56}\text{Fe}$ data from the

829 Duoplasmatron source⁶⁸. Dash black line indicates the true $\delta^{56}\text{Fe}$ value for Balmat ($\delta^{56}\text{Fe} = -$

830 0.399‰) and grey area represents the long-term reproducibility of ± 0.25 at 2SD, standard

831 deviation. February 2018 data are available in **Table S3 (supporting information B)**.

832

833

834

835

836

837

838

839

840

841

842

843

844

845

Supporting information B:

846

847 Electron Probe Microanalysis (EPMA) settings:

848 The acceleration voltage was 15kV and beam current was 15nA focused in 3 μ m.

849 Reference materials, including sulfides, oxides and silicates, were tested before the analysis

850 of S, Fe, Co, Mn, Pb, Ti, Cr, Zn, Cu and Ni. Detection limits were 133ppm for S, 130ppm for

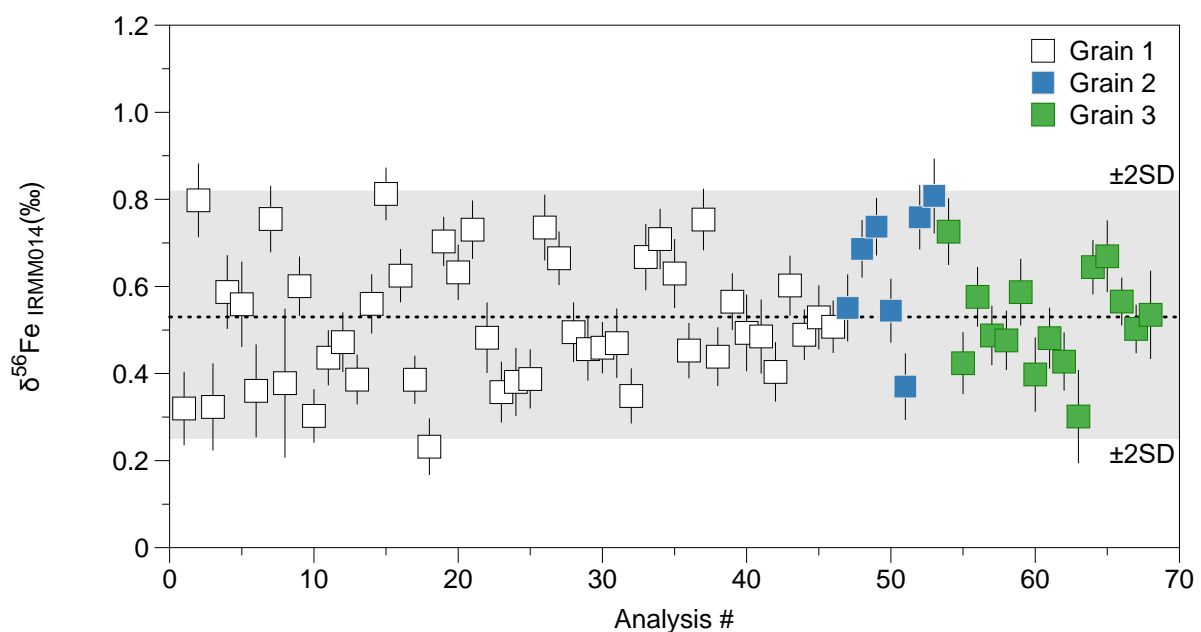
851 Fe, 141ppm for Co, 129ppm for Mn, 327ppm for Pb, 79ppm for Ti, 145ppm for Cr, 238ppm

852 for Zn, 199ppm for Cu and 150ppm for Ni.

853

854 Supplementary figures:

855



856

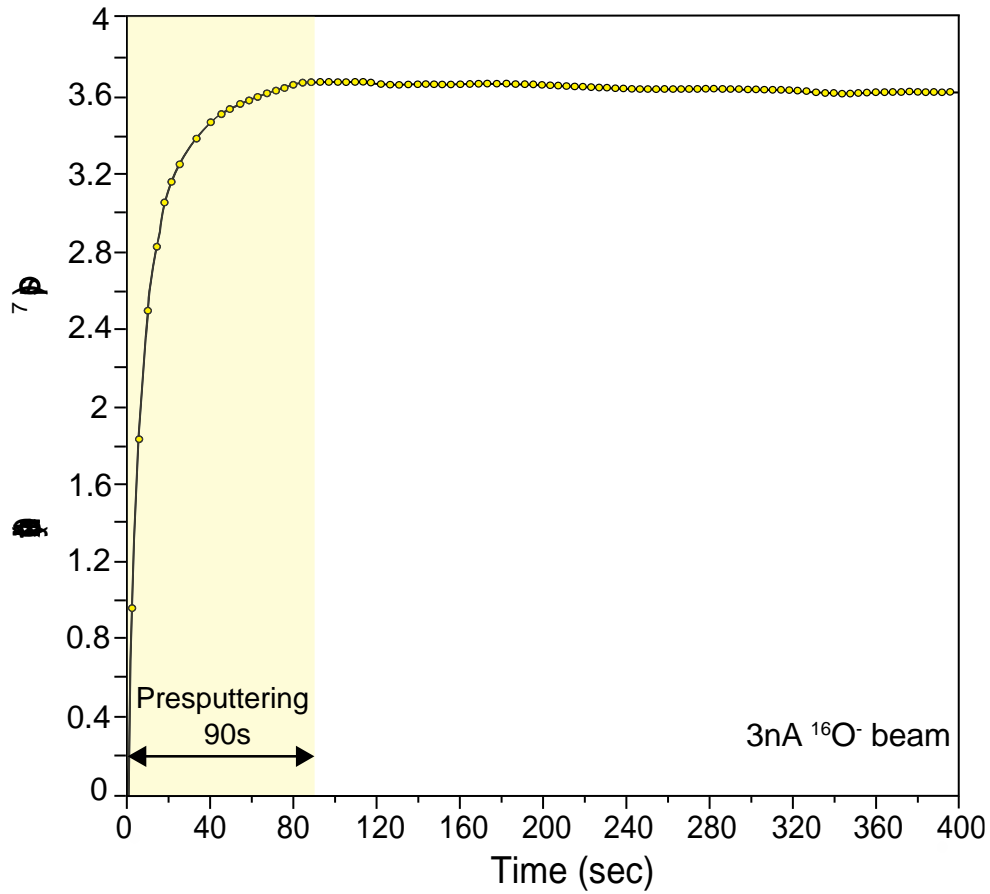
857

858 FIGURE S1 Reproducibility on Spain standard (n=68) during the July 2018 session

859 (CRPG-IPNT) in three different grains. The reproducibility is $\pm 0.28\text{‰}$ (2SD) and was

860 obtained by bracketing method. The black dashed line represents the true value of the

861 standard ($\delta^{56}\text{Fe} = +0.52\text{‰}$).



862

863

864 FIGURE S2 Intensity of $^{56}\text{Fe}^+$ in Balmat pyrite reference material obtained with Hyperion
 865 RF using a 3nA primary beam. The $^{56}\text{Fe}^+$ intensity increases and stabilizes after 90s, which
 866 corresponds to the necessary presputtering time before the analyses.

867

868

869

870

871

872

873

874

875

876

877

878

879

Analysis Name	$\delta^{56}\text{Fe}_{\text{corr}}$ ^{54}Cr	2SE	$\delta^{57}\text{Fe}_{\text{corr}}$ ^{54}Cr	2SE	$^{56}\text{Fe}^+$ intensity (cps)	$\ln(^{56}/^{54}\text{Fe})$ meas)	$\ln(^{57}/^{54}\text{Fe})$ meas)
Standards							
Balmat@8	-33.68	0.14	-50.17	0.36	3.91E+07	2.7199	-1.0647
Balmat@9	-34.10	0.13	-50.44	0.40	3.95E+07	2.7195	-1.0650
Balmat@10	-34.09	0.15	-50.63	0.41	3.95E+07	2.7195	-1.0652
Balmat@11	-33.90	0.16	-50.17	0.40	3.91E+07	2.7197	-1.0647
Balmat@12	-33.47	0.12	-49.49	0.37	4.12E+07	2.7201	-1.0640
Balmat@13	-33.69	0.12	-49.87	0.37	4.06E+07	2.7199	-1.0644
Balmat@14	-33.74	0.14	-49.77	0.39	4.08E+07	2.7198	-1.0643
Balmat@15	-33.75	0.14	-49.72	0.33	4.05E+07	2.7198	-1.0643
Balmat@16	-33.62	0.13	-49.55	0.34	4.02E+07	2.7199	-1.0641
Balmat@17	-34.10	0.13	-51.09	0.41	4.53E+07	2.7195	-1.0656
Balmat@18	-34.09	0.11	-50.94	0.30	4.54E+07	2.7195	-1.0655
Balmat@19	-34.16	0.14	-51.15	0.32	4.54E+07	2.7194	-1.0657
Balmat@20	-33.98	0.13	-50.89	0.33	4.47E+07	2.7196	-1.0654
Balmat@21	-34.16	0.13	-50.91	0.29	4.47E+07	2.7194	-1.0654
BalmatMI83@01	-33.61	0.11	-49.93	0.38	4.09E+07	2.7200	-1.0645
BalmatMI83@10	-34.12	0.13	-50.40	0.36	4.29E+07	2.7194	-1.0649
BalmatMI83@11	-34.14	0.12	-50.32	0.37	4.28E+07	2.7194	-1.0649
BalmatMI83@12	-34.06	0.15	-50.37	0.39	4.36E+07	2.7195	-1.0649
BalmatMI83@13	-33.76	0.10	-50.07	0.45	4.29E+07	2.7198	-1.0646
BalmatMI83@14	-34.14	0.12	-50.60	0.32	4.33E+07	2.7194	-1.0651
BalmatMI83@15	-34.00	0.12	-50.56	0.37	4.23E+07	2.7196	-1.0651
BalmatMI83@16	-33.79	0.12	-50.26	0.34	4.37E+07	2.7198	-1.0648
BalmatMI83@17	-34.12	0.12	-51.02	0.38	4.32E+07	2.7194	-1.0656
BalmatMI83@18	-33.77	0.13	-50.34	0.37	4.36E+07	2.7198	-1.0649
BalmatMI83@19	-33.90	0.11	-50.22	0.31	4.31E+07	2.7197	-1.0648
BalmatMI83@2	-33.45	0.13	-49.54	0.36	4.12E+07	2.7201	-1.0641
BalmatMI83@3	-33.68	0.12	-49.97	0.36	4.03E+07	2.7199	-1.0645
BalmatMI83@4	-33.86	0.11	-50.18	0.33	4.08E+07	2.7197	-1.0647
BalmatMI83@5	-33.75	0.11	-50.03	0.38	4.07E+07	2.7198	-1.0646
BalmatMI83@6	-33.72	0.11	-50.00	0.40	4.09E+07	2.7198	-1.0645

BalmatMI83@7	-34.13	0.12	-50.28	0.30	4.52E+07	2.7194	-1.0648
BalmatSTWanas@01	-33.83	0.12	-50.04	0.32	4.31E+07	2.7197	-1.0646
BalmatSTWanas@10	-33.98	0.11	-50.75	0.37	4.28E+07	2.7196	-1.0653
BalmatSTWanas@11	-33.99	0.11	-50.85	0.45	4.28E+07	2.7196	-1.0654
BalmatSTWanas@12	-33.56	0.13	-50.12	0.42	4.28E+07	2.7200	-1.0647
BalmatSTWanas@13	-33.77	0.11	-50.04	0.37	4.31E+07	2.7198	-1.0646
BalmatSTWanas@15	-33.69	0.14	-49.95	0.37	4.29E+07	2.7199	-1.0645
BalmatSTWanas@16	-33.73	0.12	-50.13	0.36	4.28E+07	2.7198	-1.0647
BalmatSTWanas@17	-33.94	0.14	-50.65	0.42	4.21E+07	2.7196	-1.0652
BalmatSTWanas@2	-34.04	0.14	-50.66	0.36	4.26E+07	2.7195	-1.0652
BalmatSTWanas@3	-34.23	0.11	-51.01	0.33	4.25E+07	2.7193	-1.0655
BalmatSTWanas@4	-34.15	0.12	-50.90	0.34	4.27E+07	2.7194	-1.0654
BalmatSTWanas@5	-33.90	0.13	-50.14	0.35	4.28E+07	2.7197	-1.0647
BalmatSTWanas@6	-34.01	0.10	-50.39	0.41	4.25E+07	2.7196	-1.0649
BalmatSTWanas@7	-33.85	0.11	-50.29	0.39	4.28E+07	2.7197	-1.0648
BalmatSTWanas@8	-33.96	0.10	-50.48	0.39	4.30E+07	2.7196	-1.0650
BalmatSTWanas@9	-33.77	0.11	-50.33	0.36	4.34E+07	2.7198	-1.0649

Samples

MI83@01	-32.96	0.14	-49.19	0.41	3.76E+07	2.7206	-1.0637
MI83@10	-32.41	0.17	-48.05	0.37	3.74E+07	2.7211	-1.0626
MI83@11	-32.54	0.13	-48.14	0.35	3.88E+07	2.7210	-1.0627
MI83@12	-33.13	0.11	-48.83	0.36	3.83E+07	2.7204	-1.0634
MI83@13	-32.33	0.15	-47.79	0.39	3.67E+07	2.7212	-1.0623
MI83@14	-33.10	0.15	-49.01	0.44	3.73E+07	2.7205	-1.0635
MI83@15	-31.74	0.13	-46.88	0.40	3.56E+07	2.7218	-1.0614
MI83@16	-32.42	0.11	-47.95	0.39	3.89E+07	2.7211	-1.0625
MI83@17	-33.12	0.13	-48.78	0.42	3.84E+07	2.7204	-1.0633
MI83@18	-32.08	0.16	-47.28	0.44	3.80E+07	2.7215	-1.0618
MI83@19	-32.73	0.12	-48.35	0.37	3.90E+07	2.7208	-1.0629
MI83@2	-32.90	0.11	-48.63	0.34	3.83E+07	2.7207	-1.0632
MI83@20	-32.54	0.15	-48.32	0.44	3.78E+07	2.7210	-1.0629
MI83@21	-31.55	0.14	-46.73	0.37	3.80E+07	2.7220	-1.0613
MI83@22	-32.32	0.11	-47.94	0.35	4.15E+07	2.7212	-1.0625

MI83@23	-31.56	0.20	-47.04	0.51	3.82E+07	2.7220	-1.0616
MI83@24	-32.09	0.15	-47.80	0.42	4.03E+07	2.7215	-1.0623
MI83@25	-31.84	0.12	-47.15	0.36	4.11E+07	2.7217	-1.0617
MI83@26	-32.03	0.13	-47.58	0.37	4.04E+07	2.7215	-1.0621
MI83@27	-31.26	0.14	-46.82	0.39	4.13E+07	2.7223	-1.0614
MI83@28	-31.59	0.13	-46.97	0.33	4.14E+07	2.7220	-1.0615
MI83@29	-32.34	0.13	-48.15	0.30	4.20E+07	2.7212	-1.0627
MI83@3	-32.00	0.13	-47.57	0.34	3.94E+07	2.7216	-1.0621
MI83@30	-31.68	0.14	-47.34	0.42	4.11E+07	2.7219	-1.0619
MI83@31	-32.61	0.13	-48.28	0.33	4.18E+07	2.7209	-1.0628
MI83@32	-32.20	0.15	-47.84	0.41	3.82E+07	2.7214	-1.0624
MI83@33	-32.65	0.19	-48.18	0.44	3.23E+07	2.7209	-1.0627
MI83@34	-32.66	0.12	-48.60	0.35	4.08E+07	2.7209	-1.0631
MI83@35	-32.57	0.16	-48.13	0.39	3.95E+07	2.7210	-1.0627
MI83@36	-32.33	0.14	-47.94	0.32	4.04E+07	2.7212	-1.0625
MI83@37	-32.04	0.12	-47.81	0.39	3.82E+07	2.7215	-1.0624
MI83@39	-31.35	0.12	-46.70	0.35	3.98E+07	2.7222	-1.0612
MI83@4	-32.71	0.15	-48.55	0.40	3.74E+07	2.7208	-1.0631
MI83@40	-30.82	0.12	-45.85	0.36	3.95E+07	2.7227	-1.0604
MI83@41	-29.48	0.34	-43.79	0.56	4.03E+07	2.7240	-1.0583
MI83@42	-31.36	0.14	-47.11	0.40	4.05E+07	2.7222	-1.0616
MI83@43	-31.87	0.11	-47.73	0.40	4.13E+07	2.7217	-1.0623
MI83@44	-30.99	0.19	-45.96	0.51	3.50E+07	2.7225	-1.0605
MI83@7	-32.34	0.14	-47.96	0.38	3.89E+07	2.7212	-1.0625
MI83@8	-32.42	0.12	-47.98	0.34	3.80E+07	2.7211	-1.0625
MI83@9	-32.28	0.13	-47.82	0.42	3.89E+07	2.7213	-1.0624
STWanas@01	-31.35	0.13	-46.69	0.34	4.23E+07	2.7222	-1.0612
STWanas@10	-31.53	0.12	-46.68	0.48	3.81E+07	2.7220	-1.0612
STWanas@11	-30.79	0.13	-45.85	0.38	4.19E+07	2.7228	-1.0604
STWanas@12	-31.11	0.13	-46.67	0.35	4.19E+07	2.7225	-1.0612
STWanas@13	-30.97	0.12	-46.31	0.34	4.22E+07	2.7226	-1.0608
STWanas@14	-31.21	0.12	-46.54	0.37	4.19E+07	2.7223	-1.0611
STWanas@15	-31.33	0.13	-46.61	0.38	4.20E+07	2.7222	-1.0611

STWanas@16	-31.29	0.13	-46.13	0.31	4.20E+07	2.7223	-1.0607
STWanas@17	-31.02	0.14	-46.16	0.38	4.26E+07	2.7225	-1.0607
STWanas@18	-30.36	0.12	-45.26	0.32	4.15E+07	2.7232	-1.0598
STWanas@19	-31.08	0.15	-46.14	0.30	4.15E+07	2.7225	-1.0607
STWanas@2	-30.91	0.11	-45.89	0.32	4.18E+07	2.7227	-1.0604
STWanas@21	-31.17	0.12	-46.37	0.35	4.23E+07	2.7224	-1.0609
STWanas@22	-31.30	0.15	-46.22	0.34	4.19E+07	2.7223	-1.0608
STWanas@23	-31.08	0.13	-46.31	0.30	4.26E+07	2.7225	-1.0608
STWanas@25	-31.21	0.12	-46.55	0.35	4.28E+07	2.7224	-1.0611
STWanas@26	-29.54	0.18	-43.80	0.42	3.64E+07	2.7240	-1.0583
STWanas@29	-31.11	0.13	-46.40	0.32	4.27E+07	2.7225	-1.0609
STWanas@30	-30.35	0.17	-45.14	0.49	3.86E+07	2.7232	-1.0597
STWanas@32	-31.03	0.10	-46.35	0.40	4.21E+07	2.7225	-1.0609
STWanas@33	-31.14	0.13	-46.30	0.40	3.63E+07	2.7224	-1.0608
STWanas@34	-31.56	0.13	-46.95	0.38	4.24E+07	2.7220	-1.0615
STWanas@35	-31.24	0.12	-46.34	0.42	4.23E+07	2.7223	-1.0609
STWanas@36	-31.24	0.14	-46.52	0.40	3.95E+07	2.7223	-1.0611
STWanas@37	-31.18	0.14	-46.42	0.38	4.21E+07	2.7224	-1.0610
STWanas@38	-31.12	0.13	-46.55	0.35	4.22E+07	2.7224	-1.0611
STWanas@39	-30.87	0.13	-46.06	0.37	4.20E+07	2.7227	-1.0606
STWanas@4	-31.62	0.13	-46.99	0.39	4.28E+07	2.7219	-1.0615
STWanas@40	-31.18	0.13	-46.68	0.38	3.92E+07	2.7224	-1.0612
STWanas@5	-31.73	0.13	-47.32	0.29	4.22E+07	2.7218	-1.0619
STWanas@6	-31.44	0.14	-46.86	0.42	4.24E+07	2.7221	-1.0614
STWanas@8	-31.33	0.12	-47.05	0.40	4.23E+07	2.7222	-1.0616
STWanas@9	-30.81	0.12	-45.78	0.32	4.25E+07	2.7228	-1.0603

880

881 TABLE S1 $\delta^{56}\text{Fe}$ and $\delta^{57}\text{Fe}$ values (corrected from ^{54}Cr interference), intensity of the
882 $^{56}\text{Fe}^+$ signal and logarithm of the measured $^{56}\text{Fe}/^{54}\text{Fe}$ and $^{57}\text{Fe}/^{54}\text{Fe}$ ratios in Balmat pyrite
883 standard and geological samples (pyrites) during July 2020 session (SwissSIMS). The 2SE
884 (standard error) reports the internal uncertainty.

885

886

887

Analysis Name	$\delta^{56}\text{Fe}_{\text{RAW}}$ (‰)	$\delta^{56}\text{Fe}_{\text{IRMM014}}$ (‰)	2SE
X-Y test			
Position 0° (P0)			
Balmat@25	-31.71	-0.52	0.09
Balmat@26	-31.77	-0.58	0.11
Balmat@27	-31.60	-0.41	0.09
Balmat@31	-31.38	-0.20	0.10
Balmat@32	-31.48	-0.29	0.11
Balmat@33	-31.44	-0.26	0.12
Position 90° (P1)			
Balmat@34	-31.48	-0.30	0.10
Balmat@35	-31.69	-0.50	0.10
Balmat@36	-31.86	-0.67	0.12
Position 180° (P2)			
Balmat@38	-31.49	-0.31	0.10
Balmat@39	-31.60	-0.41	0.10
Balmat@40	-31.60	-0.41	0.12
Position 270° (P3)			
Balmat@45	-31.82	-0.64	0.11
Balmat@46	-31.70	-0.51	0.10
Balmat@47	-31.41	-0.22	0.12
Balmat@48	-31.45	-0.26	0.12
Balmat@49	-31.49	-0.30	0.09
Crystal orientation test			
Grain #1 (G1)			
BalmatG1 @38	-29.81	-0.12	0.12
BalmatG1 @39	-29.92	-0.23	0.12
BalmatG1 @40	-30.21	-0.52	0.10
BalmatG1 @41	-29.94	-0.25	0.13
BalmatG1 @43	-30.01	-0.32	0.11

Grain #2 (G2)

BalmatG2@9	-30.25	-0.57	0.11
BalmatG2@10	-30.31	-0.62	0.10
BalmatG2@11	-30.43	-0.74	0.10
BalmatG2@12	-29.93	-0.24	0.10
BalmatG2@13	-30.45	-0.76	0.13

Grain #3 (G3)

BalmatG3@24	-30.09	-0.41	0.09
BalmatG3@25	-30.20	-0.51	0.10
BalmatG3@26	-30.18	-0.49	0.11
BalmatG3@27	-29.69	0.00	0.10
BalmatG3@28	-29.88	-0.20	0.10

Profile Pf1

BalmatPf1@01	-27.37	-0.27	0.11
BalmatPf1@02	-27.62	-0.52	0.12
BalmatPf1@03	-27.52	-0.42	0.12
BalmatPf1@04	-27.60	-0.50	0.10
BalmatPf1@05	-27.50	-0.41	0.11
BalmatPf1@06	-27.49	-0.40	0.13
BalmatPf1@07	-27.49	-0.39	0.12
BalmatPf1@08	-27.38	-0.28	0.12

888 TABLE S2 Raw $\delta^{56}\text{Fe}$ and IMF-corrected $\delta^{56}\text{Fe}$ values measured by SIMS on Balmat
889 pyrite in four different position (0° , 90° , 180° and 270°) to test orientation (channeling) effect
890 (data acquired during September 2020 session); in three Balmat grains mounted in random
891 orientations to test a possible crystal orientation effect (data acquired during September 2020
892 session); and a core to rim profile in a Balmat grain. The internal uncertainties of the
893 measurements are reported as 2SE.

894

895

896

Analysis Name	$^{56}\text{Fe}^+$ intensity	$\delta^{56}\text{Fe}_{\text{RAW}}$ (‰)	$\delta^{56}\text{Fe}_{\text{IRMM014}}$ (‰)	2SE
Balmat-3nA@22	6.13E+07	-33.50	-0.38	0.09
Balmat-3nA@23	6.09E+07	-33.50	-0.38	0.10
Balmat-3nA@24	5.97E+07	-33.60	-0.48	0.08
Balmat-3nA@25	6.23E+07	-33.53	-0.41	0.10
Balmat-3nA@26	6.17E+07	-33.47	-0.35	0.10
Balmat-3nA@39	6.11E+07	-33.39	-0.23	0.08
Balmat-3nA@40	6.18E+07	-33.52	-0.36	0.11
Balmat-3nA@41	6.07E+07	-33.38	-0.22	0.10
Balmat-3nA@42	6.27E+07	-33.45	-0.29	0.10
Balmat-3nA@43	6.33E+07	-33.77	-0.61	0.09
Balmat-3nA@44	6.21E+07	-33.66	-0.50	0.09
Balmat-3nA@45	6.32E+07	-33.75	-0.59	0.07
Balmat-3nA@50	6.63E+07	-33.97	-0.63	0.09
Balmat-3nA@51	6.31E+07	-33.65	-0.30	0.11
Balmat-3nA@53	6.12E+07	-33.57	-0.22	0.09
Balmat-3nA@54	6.47E+07	-33.79	-0.44	0.08
Balmat-3nA@55	6.28E+07	-33.90	-0.55	0.08
Balmat-3nA@56	6.32E+07	-33.61	-0.26	0.09
Balmat-3nA@57	6.51E+07	-33.44	-0.50	0.09
Balmat-3nA@58	6.48E+07	-33.11	-0.18	0.09
Balmat-3nA@59	6.57E+07	-33.31	-0.38	0.08
Balmat-3nA@60	6.53E+07	-33.29	-0.36	0.08
Balmat-3nA@61	6.66E+07	-33.51	-0.58	0.10
Balmat-3nA@62	6.37E+07	-33.35	-0.41	0.07
Balmat-3nA@63	6.28E+07	-33.45	-0.51	0.13
Balmat-3nA@64	6.26E+07	-33.19	-0.25	0.09
Balmat-3nA@65	6.09E+07	-33.26	-0.32	0.10
Balmat-3nA@66	6.30E+07	-33.43	-0.49	0.09
Balmat-3nA@67	6.58E+07	-33.34	-0.41	0.07
Balmat-3nA@69	6.64E+07	-33.50	-0.47	0.09
Balmat-3nA@70	6.44E+07	-33.48	-0.46	0.10

Balmat-3nA@71	6.73E+07	-33.35	-0.32	0.09
Balmat-3nA@72	6.63E+07	-33.37	-0.35	0.10
<hr/>				
Mean IMF (‰)		-33.10		
Mean Repro (‰,				
2SD)		0.39		
Repro. bracketing (‰, 2SD)		0.24		

897

898 TABLE S3 $^{56}\text{Fe}^+$ intensity, raw and IMF-corrected $\delta^{56}\text{Fe}$ values associated with Balmat
899 pyrite standard analyses (February session in CRPG-IPNT, $^{57}\text{Fe}/^{54}\text{Fe}$ ratios were not acquired
900 during this session). The internal uncertainties are given as 2SE.

901

902

903

904

905